2016

Design, Fabrication, and Characterization of a Gun-Launched Deployable-Wing Unmanned Aerial System

Timothy Schutter
Lehigh University

Design, Fabrication, and Characterization of a

Gun-Launched Deployable-Wing Unmanned Aerial System

By

Timothy Schutter

A Thesis

Presented to the Graduate and Research Committee

of Lehigh University

in Candidacy for the Degree of

Master of Science

in

Mechanical Engineering

Lehigh University

September 2016

This thesis is accepted and approved in partial fulfillment of the requirements for the Master of Science.

_____

Date

_____

Keith W. Moored, Thesis Advisor

_____

Terry J. Hart, Co-Advisor

_____

D. Gary Harlow, Chairperson

Department of Mechanical Engineering and Mechanics

Acknowledgements

Table of Contents

Table of Figures

List of Tables

Abstract

With the miniaturization of electronics and leaps in battery energy storage technology there has been renewed interest in unmanned aerial systems (UAS). UAS present an opportunity for soldiers to enhance their situational awareness via significantly increased battlefield surveillance. The structure of a UAS is frequently fragile and requires care when handling. Additionally, many UAS use launch mechanisms that require additional training, incur a weight penalty for the soldier and use on-board energy to reach their surveillance altitude. The gun-launched UAS (GLUAS) eliminates these shortcomings by utilizing an existing gun for launch, and packaging the platform inside a round that is already a standard piece of equipment carried by the soldier.

The 40 mm and 60 mm ammunition round are excellent platforms on which to develop a gun-launched UAS. Once launched, the GLUAS will rise to apogee where the outer shell will be released and the wings and propeller will deploy. There will be integrated control surfaces, an integrated autopilot and on-board cameras allowing the GLUAS to maneuver and survey the battlefield.

We have developed a prototype design that lays the foundation for the successful development of a GLUAS. The prototype incorporates a multi-section, folding wing with elevons as the control surfaces. Initial flight tests of a scaled model have demonstrated that the flat-plate, low aspect ratio planform prescribed by the packaging constraints is a flight-worthy platform for this versatile surveillance package.

1. Requirements

The gun launched UAS must be able to support the high forces experienced during gun launch, which are up to 20,000 g. It must then fly fully autonomously or with guidance from a laptop computer operated by a soldier on the ground. The constraints further require that the GLUAS have a range of 8 to 10 kilometers and be able to be packaged in the same space as a standard mortar round including the wings, propeller and all electronics.

The airframe chosen must provide sufficient lift to support the payload, electronics and batteries of the GLUAS. While generating lift, it is crucial to minimize drag so that the GLUAS can achieve the required range. Additionally, the wing should facilitate stable flight and have the appropriate control surfaces to maneuver the aircraft as the pilot commands. It is also important that the final product have a unit cost of $100 once it is mass-produced.

1.2 Literature Review

There have been a fair number of impulse launched UAVs in recent years. Some have been gun-launched and others have been built into rockets. A project at MIT in 1998 produced a gun-launched surveillance UAV for the NAVY called the WASP (Wide Area Surveillance Projectile). It was designed to be launched from a 5-inch gun with a flight time of 15 minutes. When the structure was launched, a parachute would pull the UAV from the shell and the wings would deploy. The wings were a folding, high aspect ratio

(AR) design with a modified T16 airfoil. A conventional tractor propeller was mounted to a 0.42 horsepower gas engine on the nose cone of the shell to provide thrust at an anticipated cruising velocity 38.6 m/s. The design went through wind tunnel and flight testing and was ruled as success [1]. A group from the University of Dayton designed a 60 mm grenade launched UAV. This UAV had a tractor propeller for powered flight and a torsion spring leading edge that would open the fabric membrane wings. The design was a large Zimmerman wing with a conventional empennage immediately behind the wing. There were no control surfaces on the wings so the UAV was designed to be launched from a small rocket and then spiral back down to the ground. They achieved varying degrees of success in test flights [2]. A rocket based inflatable UAV was designed at Oklahoma State University. The UAV is composed of a rocket with inflatable wings that deploy at apogee turning the projectile into a fixed wing structure. The thrust in the fixed wing configuration is provided by an electronically ducted fan which supports the 72 inch wing span and 12 pound flight weight at cruise. In testing, flutter destroyed the control surfaces on the wings, but the CO_2 filled wings remained inflated [3].

There are multiple wing styles for the deployable UAV. These include rigid, inflatable and membrane wings. With each of these wing types, there are many wing shapes that can be achieved, each with some merits and drawbacks. Additionally, for types of lifting mechanisms, there are fixed wings, rotary wings (like the blade on a helicopter) and flapping wings. The fixed wing is the most efficient for applications that don't require

3

hovering. For hovering the rotary wing is preferred for higher flight speeds while flapping is better for lower flight speeds [4].

An important aspect of small UAV and MAV flight is the Reynolds numbers that they operate at, which are low Reynolds numbers in the range of $Re = 1X10^5$ for MAVs. Pelletier and Mueller studied a 6 inch wing with AR values ranging from 0.5-3 inch. These were thin, flat and cambered models with a 1.93% thickness-to-chord ratio. They found that no hysteresis was present and that the wings did not experience an abrupt stall. The cambered airfoil had an improved lift coefficient but also increased the drag coefficient. They also found that the leading and trailing edge geometries did not have a significant effect on these coefficient in terms of their elliptical shape or taper [5]. There are three sources of lift on low AR low Reynolds number wings which are the lift from circulation, from tip vortices and from leading-edge vortices in the case of high sweep angle delta wings. In wind tunnel testing of rectangular, elliptical Zimmerman and Zimmerman wings it was found that for higher AR wings, the lift curve remained more linear up to the stall angle, and that the transition from non-linear to linear lift occurred at $AR = 1.25$. The models tested had 5-to-1 elliptical leading and trailing edges and thickness-to-chord ratios of 1.96% and 2.60%. All cross-sections were flat plate airfoils [6]. The original shape of the GLUAS incorporated wings with a higher sweep ratio that were similar to a delta wing. Delta wings have been found to have low lift to drag ratios at subsonic speeds but also have lift coefficients that increase up to high angles of attack. The wings tested had 45 and 60° sweeps and $Re = 3.5x10^{\wedge}5$. The first was a NACA0012 and the second was a flat plate

4

with a sharp leading edge. These experiments experienced hysteresis where the leading edge vortex started from the trailing edge and worked its way forward [7]. This vortex is something that is associated with high lift coefficients at high angles of attack, but is not applicable to the GLUAS as it is not a delta wing. The GLUAS is closer to a Zimmerman planform so the characteristics expected are those of a Zimmerman.

There are many wing technologies to enhance aerodynamic characteristics. The important factors are lift, drag, stability and controllability. Morphing wings and deployable wings are two separate technologies that are frequently used in small UAVs. A deployable wing is a wing that opens from a closed and unused position, usually inside the fuselage, to an open position where they interact with the surrounding airflow. A morphing wing is one that goes through a shape change to manipulate its aerodynamics. This can be to control the attitude of the plane or to change the flight characteristics for varied flying speeds. The work of Bristol and Virginia Tech discusses morphing. The morphing mechanism needs to be a part of the wing structure. They have worked with telescoping wings and varying sweep wings along with aeroelastic tailoring and truss structures. They found that controllers need to be able to handle the coupled control that results from the changes in wing shape [8]. University of Florida has worked on a MAV having a conventional wing and tail configuration with plastic membrane wings what have a carbon fiber leading edge and carbon fiber battens. They use servos connected to torsion rods to warp the trailing edge of the wing. In flight tests, it responded well in roll to the wing warping [9]. There has been lots of interest in non-traditional actuation devices. In 2001 there was interest in

5

using Microelectromechanical systems to control the control surfaces on micro fixed wing vehicles and their potential to be activated such that they could energize boundary layers and delay separation. It was determined to be a viable possibility [10]. Macro-fiber-composite actuators have been tested in place of elevons on the trailing edge of a morphing wings. They resulted in lower drag and increased performance. The lift-to-drag ratio was almost always improved with the use of these actuators. A model with these components was also flown on a 0.76 m wing span UAV [11]. The Air Force Research Lab (AFRL) found in experiments that wing flexures increase the maximum lift-to-drag ratio by 20-30% for speeds of 20-50 miles per hour. With an AR of 6.16 and a span of 24 inches they found that the stall angle increased by 40%. They also found that the airframe had good stability in the three control axes [12].

There have been many design configurations built and tested involving deployable wings. The two most common types are inflatable wings and folding wings. There are design tradeoffs that must be considered between these two types of deployable wings. Inflatable wings are limited by the weight that they can carry before creasing and folding wings are constrained by the volume into which they must collapse [13]. Inflatable wings on airplanes date back to 1957 with the Goodyear Inflatoplane. Modern inflatable wings tend to use high pressure inflatable spars. Modern, high strength braided fibers make it possible to achieve these higher pressures. [14]

All of these different configurations can be used in the design of a UAV. It is important to know what characteristics are required before selecting features. A group in France have

built a biplane MAV. They found that it produced less induced drag for a given amount of lift but that the parasitic drag increased. Their conclusion was that this could be a good platform for low speed and heavy lifting situations and that it had better aerodynamic performance than a plane with a single fixed wing. The inverse Zimmerman biplane that was tested in the wind tunnel also benefited from having the flow of the propeller air over the wing when it was placed in the trailing edge of the top wing [15]. AeroVironment Inc. built the Black Widow in 2001 which is a commonly referenced MAV. It flies at 30 mph and has an endurance of 30 minutes. It is a vaguely elliptical fixed wing with three vertical stabilizers on the trailing edge and a tractor propeller hanging off the leading edge. The Black Widow has shown that a 6 inch wing span, 80 gram MAV is possible [16]. In reducing the size of their low AR twin propeller MAV called "Bidule", a group from Sydney Australia looked into the effects of the propeller wash on the MAV. They determined that the lift was improved with the propeller wash, but that the wash can also cause stability issues [17]. Both of these effects are very important as the propeller frequently covers a large region of the wing on small UAVs unlike large scale aircraft. This is something that appears to be an issue with the GLUAS, but will be discussed more in the section on flight testing.

University of Maryland found that on a log-log plot of wing span and endurance that all MAV fall on a linear line. For UAVs in the 100-500 gram range typical endurance is 10-25 minutes [18]. The GLUAS falls in this region at 349 grams with an anticipated endurance of just under 22 minutes.

2. Design

The GLUAS must have a deployable wing in order to fit within the 60 mm mortar shell dimensions and to maintain altitude during flight. This wing needs to have integrated control surfaces, be deployable during flight and be able to withstand flight wing loadings and the immense initial load of launch from the gun. This means that there must be a great deal of strength in the structure to handle these tremendous loads that are not normally encountered by UAS components. The result, necessarily, is an increase in weight, which needs to be held to a minimum to reduce negative effects on flight characteristics and performance goals.

2.1 Initial Design

Many design methods were considered to achieve these specification. These included fabric wings, inflatable wings and rigid folding wings. Due to the necessity to build a controllable UAS, fabric and inflatable wings were rejected as they cannot easily use conventional control surfaces and would require wing warping. A rigid wing structure was chosen for this reason.

The design of the GLUAS is based around a folding wing structure. The basis for the design has been passed along from the group previously working on this concept and is the starting

point from which the rest of the research is derived. Each wing is composed of five wing sections that fan open from a common pivot point to produce the full wing. The result is an airframe that is essentially a flying wing. One wing section on each side has a control surface for pitch and roll control known as an elevon. The elevon is controlled through a control horn and connecting rod by a servo mounted in the fuselage of the GLUAS. Due to the constraint that the wings must fold into the fuselage, the control surface is located on a single wing section and has an aspect ratio of less than 1. When this project was passed on to our group the initial concept was formed but not fully developed. A 40 mm model had been tested in the wind tunnel and a second model with folding wings actuated by linear springs had been manufactured and assembled. This model is shown in Figure 1 with its wings deployed, but the elevons are absent from the model in this picture. A method for actuating the elevons had not been conceived at this point. Flight was never attempted or considered with this model.

Figure 1: GLUAS Model 1 with 3D printed fuselage and aluminum wings

The UAV has gone through multiple design and fabrication iterations. Initially the design specifications were for a 40mm ammunition round. This model was very small and would require extremely tight packing of very small components. The original model was built for these constraints. It was very simple, having only wings, a fuselage, vertical stabilizer and a motor. The lift and drag of the model were measured in order to characterize its performance. A foam version that was at 3 times the scale of the 40mm design, or 120mm, was used to test its stability and controllability in flight. This model was flown and confirmed that the planform and control surfaces produced a solid platform to build upon. At this point a second model was requisitioned which would be designed around a 60mm mortar round. Due to the increased size, it made sense to design and build prototypes of

this larger size and later scale everything down further to 40mm after the model was proven to be functional. The emphasis of work was then focused on the 60mm model.

2.2 Packing the GLUAS into a Mortar Shell

With the wings and tail collapsed, the GLUAS fits into a metal tube. This tube connects to the tail section of a mortar round and in addition to holding the GLUAS, it also provides a method to transport the launch force from the tail section to the structural support near the front of the GLUAS. Only the front of the fuselage and the motor protrude from the metal tube. Figure 2 shows the GLUAS inside a 60mm tube that is connected to the mortar tail section.
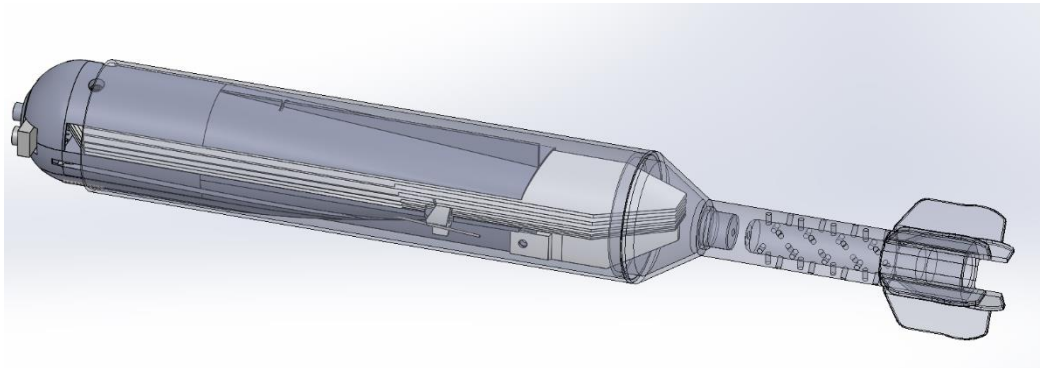
Figure 2: GLUAS packaged in mortar shell

3. Analysis of Aerodynamic Characteristics

In order to shape the design of the GLUAS, the first action was to examine the influence of the individual components in order to configure them to yield the most favorable performance. Some of the characteristics were confirmed experimentally while others were calculated based on logical assumptions. A model was evaluated in a wind tunnel to collect lift and drag coefficient measurements to establish a basis of the aerodynamics upon which to build. Range, endurance and other requirements for flight were calculated theoretically from these measurements. Field test flights were used to prove that the calculations and data from the steady state wind tunnel conditions translated to realistic flight conditions, which now appear to be 10-13 m/s.

3.1 Lift and Drag

Two of the important figures for this project are endurance and range. These numbers are significant for a surveillance platform to be able to collect as much data as possible. The endurance is a measure of the maximum time that an aircraft can stay aloft, while the range is the maximum distance it can travel.

The equations for range and endurance are:

$$Endurnace = \frac{m_{batt}E_{density}\eta}{W_{total}^{3/2}}\left(\frac{CL^{3/2}}{C_D}\right)\sqrt{\frac{\rho S}{2}} \qquad\qquad [19]\ (1)$$

$$Range = E_{density}\eta\left(\frac{C_L}{C_D}\right)\left(\frac{m_{batt}}{W_{total}}\right) \qquad\qquad [19]\ (2)$$

12

where m_{batt} is the battery mass, $E_{density}$ is the energy density of the battery, η is the total efficiency, W_{total} is combined weight of the structure and battery, C_L is the lift coefficient, C_D is the drag coefficient, ρ is the density of the air and S is the surface area of the wings. The lift and drag coefficients that can be determined experimentally in the wind tunnel are important elements of these two equations. Depending on whether the goal is to maximize the endurance or to maximize the range of the UAS, it becomes important to fly at the angle of attack that corresponds to the highest value of either $C_L^{3/2}/C_D$ or C_L/C_D respectively. In order to determine these values the lift and drag curves must first be determined.

The wind tunnel that was used to study the GLUAS was a low speed wind tunnel. Speeds ranging from 1.5 m/s to 40 m/s are achievable in the closed-loop configuration. The acrylic test section is 46 by 46 cm and 81 cm long. The GLUAS was secured to a pivoting extension that was mounted to an AEROLAB sting balance, Figure 3. The pitch of the models was adjusted manually using two screws to affix the required angle of attack. A digital level was held against the top surface of the fuselage to confirm that the specified angle was achieved. A result of this manual adjustment was that the true angle of attack values varied by up to one (0.5) degree from their intended values. Once the angle of attack was set, the values of the normal and axial forces were tared to have a zero point for the force measurements. At this point the wind tunnel was turned on and the wind speed was adjusted to the predetermined values and data was collected at each wind speed. When the range of speeds was completed, the wind tunnel was shut down, the angle of attack was adjusted to the next value and the sensor values were once again tared before repeating the

13

process. The data was taken for full scale wind speeds ranging from 4.5m/s to 18m/s with a full scale root chord length of 15.5 cm and Reynolds numbers from 4.3×10^4 to 1.7×10^5. Here the term "full scale" references the dimensions of the 40 mm model as scaled models were also tested. Angles of attacked ranged from 0° to 45°. All of the data was passed through a National Instruments DAQ NI 2919 and acquired with LabView.
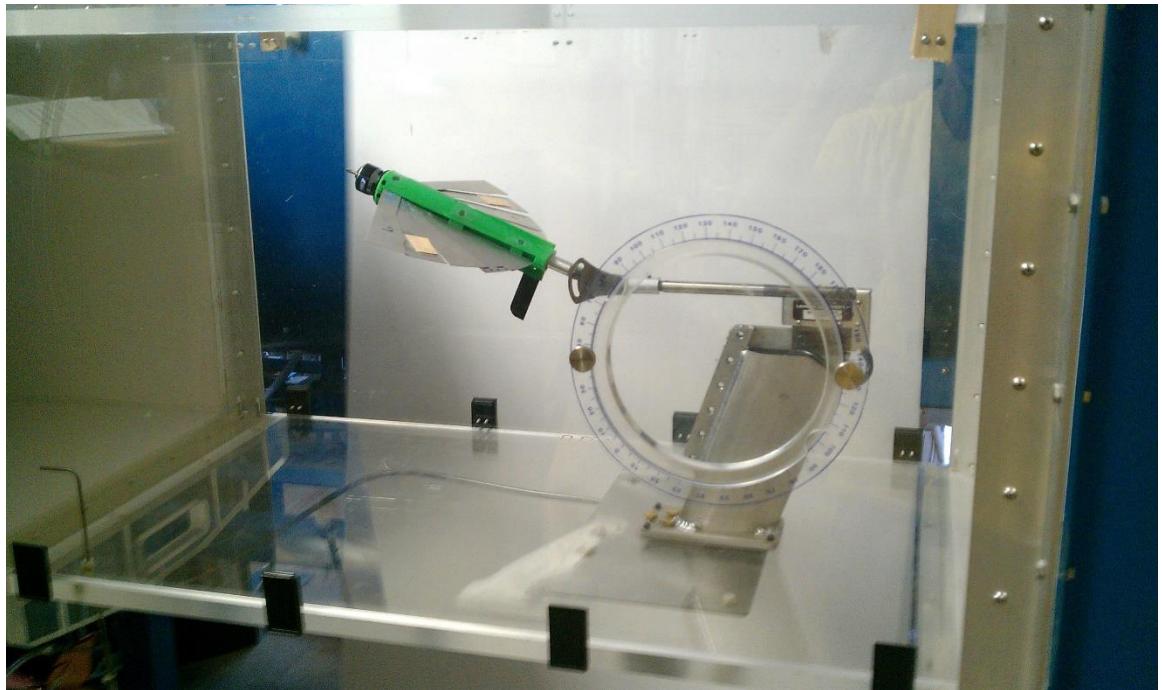
Figure 3: AeroLab sting balance shown with 40mm GLUAS model

Two different scaled models were analyzed in the wind tunnel. Neither model had a powered propeller nor functional control surfaces. As a result, only lift and drag of the wing-fuselage-combination were measured and the effects of propeller wash were not examined.

Figure 4: 40mm Model in Wind Tunnel at 10 degrees and 13.4 m/s

The initial model was a modified 40mm design to allow mounting. It was run at 13.4 m/s or a root chord Reynolds number, Re $= 1.4\text{x}10^5$, in 2.5° increments from $-15°\alpha < 15°$ and in 5° increments from $-20° < \alpha < 40°$. In positive angles of attack, the wing sections began to separate from the aerodynamic loads acting on them (see Figure 4). The blur of the two leading wing sections was the result of flutter. A thin strip of balsa wood was used to hold the elevons in their neutral position or else they experienced a great deal of flutter due to the fact that they were hanging, unsupported from the wing sections. The bending of the wing sections increased with increasing angle of attack.
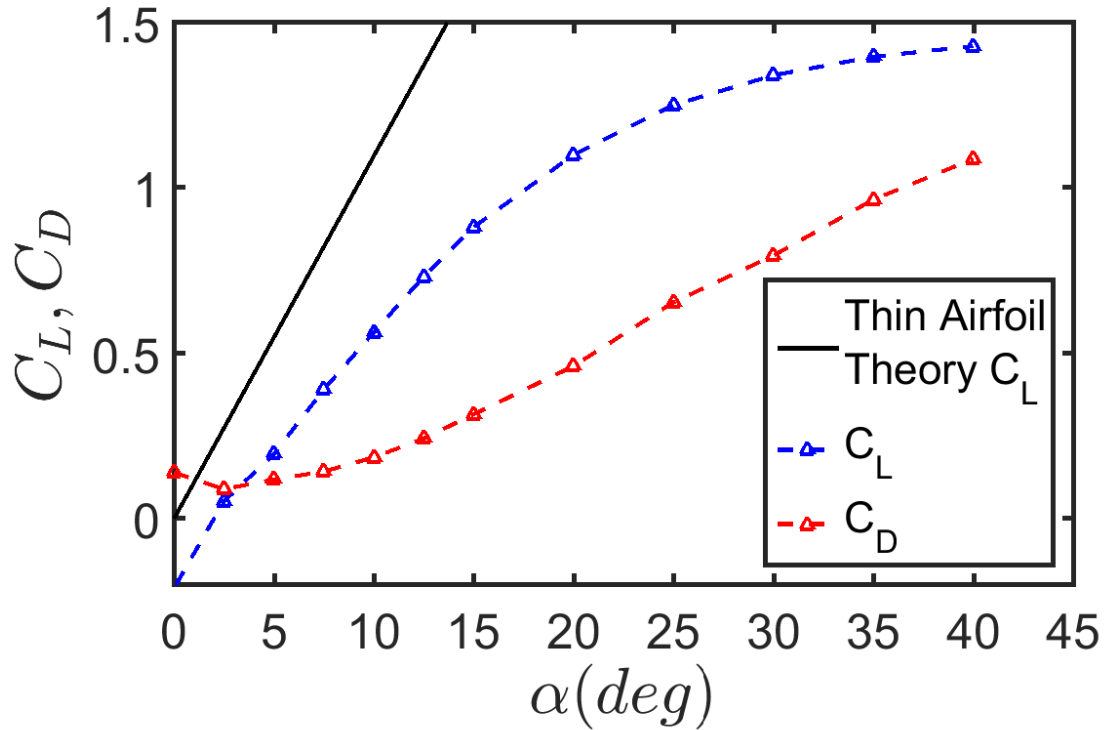
Figure 5: C_L, C_D as a function of angle of attack for *40* mm GLUAS with separating wing sections

Figure 5 shows that the lift coefficient is about half of what thin airfoil theory predicts up to $\alpha = 15°$, after which, it increases more slowly. The lift coefficient increases all the way up to $\alpha = 40°$. This result prompted future testing to take place with a smaller model in an attempt to reduce any wall and blockage effects. The coefficient of lift is negative at $\alpha = 0$. This is unexpected due to the fact that the stacking order of the wing sections causes the leading edge of the wing near the root to have a positive angle of attack when the fuselage is level. The coefficient of drag follows the typical quadratic curve seen in airfoil testing.
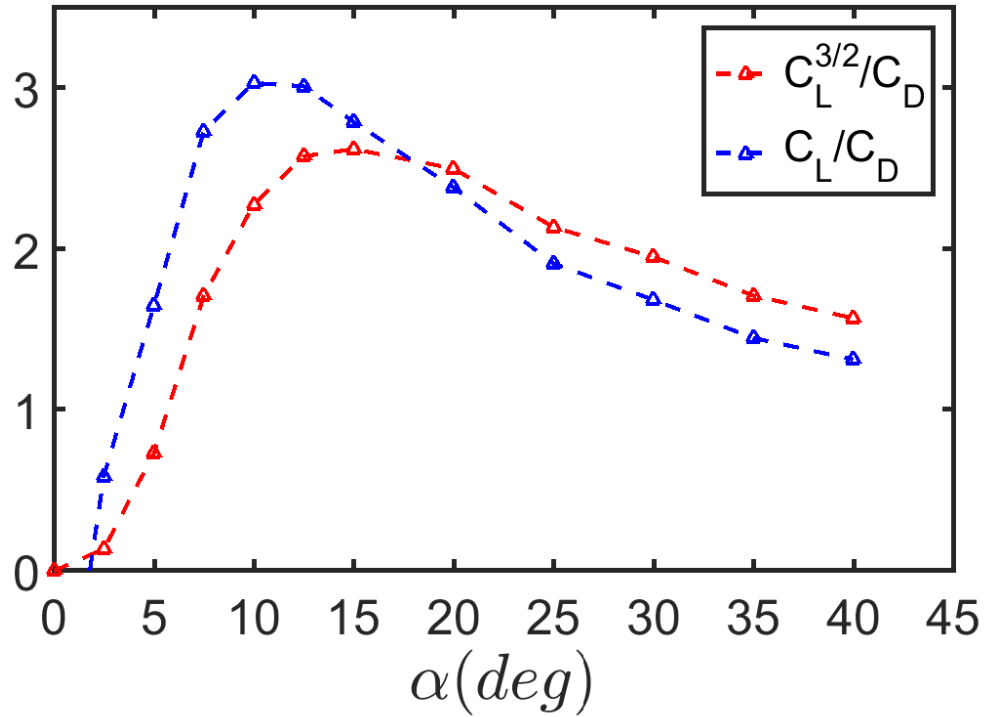
Figure 6: $C_L^{3/2}/C_D$ and C_L/C_D as functions of angle of attach for 40mm GLUAS with separating wing sections

Values of $C_L^{3/2}/C_D$ and C_L/C_D are shown in Figure 6. The value of $C_L^{3/2}/C_D$ peaks at $\alpha = 15°$ but is relatively constant between $12.5° < \alpha < 20°$ in the 2.5. The value of C_L/C_D peaks at just over 3 at $\alpha = 10°$.

The second model was a half scale of the 40mm model. This was based off of a new 40mm design so it is not exactly half the size of the original 40mm model. The reason that the model was scaled down was because it was getting close to the top wall of the wind tunnel

17

at high pitch angles and it was necessary to determine if wall effects were the cause of the plateau in the lift coefficient data. Also, the reduced size meant that inside of the 18 by 18 inch test section in the wind tunnel it would only have a blockage effect of about 2.4% instead of 9.6% when the model was pitched to an angle of attack of 45°. The justification for doing this was because previous testing of the full scale 40 mm model had shown that the lift coefficient continued to increase all the way up to $\alpha = 40°$ and it was important to know if this was an effect of the planform or wall effects. The wind speed was changed in order to hold the Reynolds number constant and the thickness of the wing sections were adjusted such that they would bend proportionally to the full scale model. A variety of wind speeds were tested to get an idea of the aerodynamic characteristics at different Reynolds numbers.

In order to keep the aerodynamic effects of the half scale model representative of the 40mm model it was necessary to keep the Reynolds number constant.

$$Re = \frac{\rho V c_{Root}}{\mu} \tag{3}$$

Here ρ is the density of air, V is the free stream velocity, c_{Root} root chord of the wing and μ is the dynamic viscosity of air. In order to keep the Reynolds number constant when L was half its original value, the velocity, V, needed to be doubled. Next it was necessary to scale the aeroelastic effects so that the half scale airframe would behave just like the full scale model. For this it was necessary to determine the effective stiffness which is a function of the bending forces divided by the fluid forces. Starting with the bending forces:

$$M = EI\frac{d^2y}{dx^2} \qquad (4)$$

Where M is the moment in a beam, E is the modulus of elasticity, I is the second moment of the area, and d^2y/dx^2 is the bending curvature of the wing. By integrating twice and collecting terms, the result is:

$$F \propto \frac{EI}{L^3}y \qquad (5)$$

Using the non-dimensional $y* = y/L$ and the fact that $I \propto t^2w$ where t is the thickness of the wing section and w is the width, the bending force is found:

$$F_{Bending} \propto \frac{Ewt^3}{L^2} \qquad (6)$$

The effect of the fluid forces is:

$$F_{Fluid} \propto \rho V^2 A \qquad (7)$$

The result is:

$$\pi = \frac{F_{Bending}}{F_{Fluid}} = \frac{Ewt^3}{L^2\rho V^2 A} \qquad (8)$$

Using half the wing section width, w, and half the wing section length, L, of the previous model, it worked out that the wing thickness should be 0.79 times the thickness of the previous wings in order to experience the same wing deflections.

During testing in the wind tunnel, it was evident that changing the stacking order of the wing sections effected the wing shape under load. With the wings stacked such that the leading wing section was on the bottom, the wing sections were pushed together as the angle of attack increased and the result was a continuous wing that was forced into a dihedral shape from the aerodynamic forces applied to it. If, on the other hand, the wing sections were stacked such that the leading one was on top, the sections would separate. The sections closest to the leading edge separated the most and the last section bent only a slightly. In the case where the wing sections separated, there was more dihedral present than in the case where they did not separate. It appears that this was because the load was more evenly distributed when the sections were together, when the higher load of the leading wing sections was distributed to the trailing sections that experienced less of their own load and so the total dihedral was reduced. A comparison of the two configurations is shown in Figure 7.
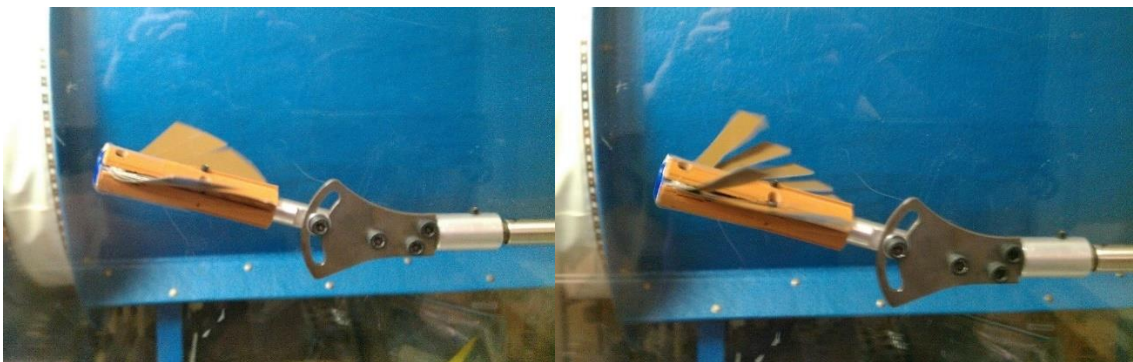
Figure 7: (a) Continuous wing. (b) Separating wing.

The case with the separation resulted in flutter of the two lead leading sections, but it did not appear that this flutter increased the drag on the GLUAS. In the following figures the solid line represents data from the continuous wing stacking arrangement and the dashed line represents data from reversed stacking which resulted in the wing sections separating.
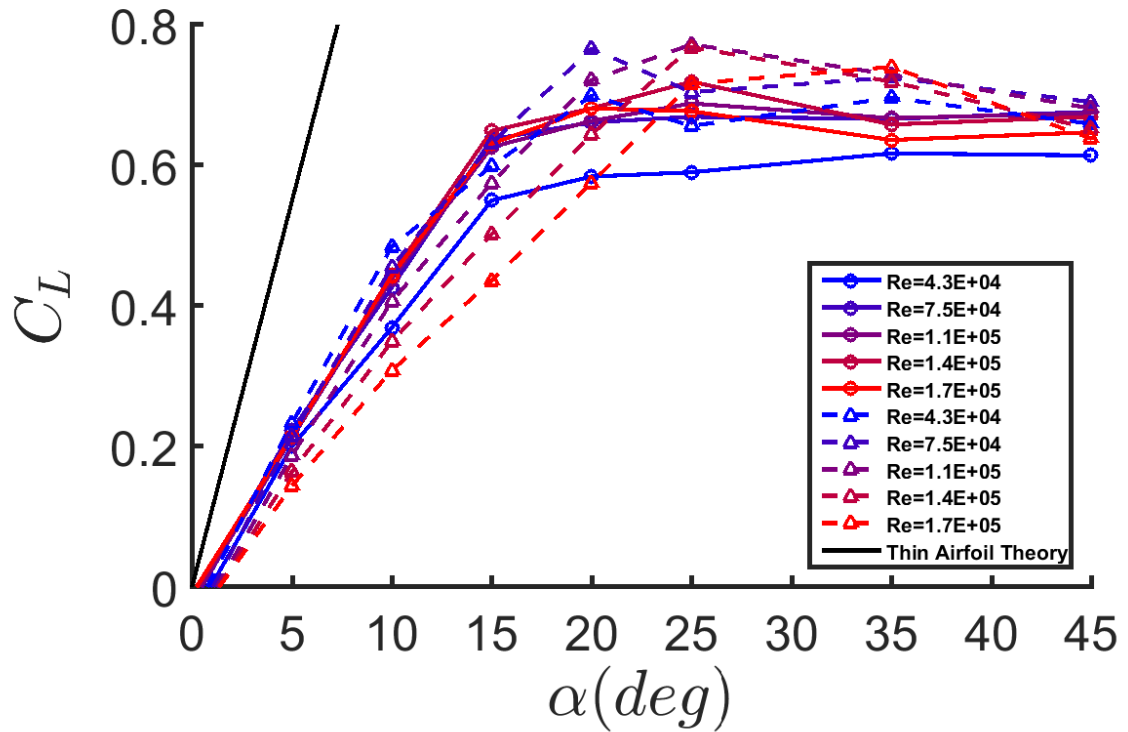
Figure 8: C_L as a function of α comparison of five-section continuous and separating wings

In Figure 8, the experimental lift coefficient is significantly lower than the value predicted by thin airfoil theory. The continuous wing produces very similar values at low angles of attack while the separating wing has a larger range of values. In these low angles the lift

coefficient is reduced with increasing Reynolds number. Where $15° < \alpha < 20°$, the separating wing begins to yield a higher lift coefficient value than the continuous wing. At $\alpha = 25°$, a new trend appears where the mid-range Reynolds numbers produce the highest lift coefficients, and this is evident for both stacking configurations. As the angle of attack is increased past 25°, the lift coefficient for the separating wing slowly decrease while the lift coefficient for the continuous wing remains relatively constant. The values for these two different arrangements converge to the same values at $\alpha = 45°$. Compared to the 40 mm model with separating wing sections where the lift coefficient continued to rise past $\alpha = 25°$, the half scale model with separating wing sections shows that the lift coefficient remained constant and even began to decrease for some wind speeds. This points to the fact that there was something different between the two configurations. More than likely this was a result of moving the model away from the wall and reducing the influence of the wall effects. The separating wing produced less lift at low angles of attack than the continuous wing for the higher Reynolds numbers. This could be a result of the wing sections bending more in the separating wing case and effectively lowering the wing span, thus reducing the lifting surface. The fact that it is most evident at the highest Reynolds number when the wing sections were bending the most supports this idea. The separating wing produces the highest lift coefficients. This is very possibly the result of the wings separating and allowing the free stream air to inject momentum into the boundary layer of each wing sections thereby increasing lift.
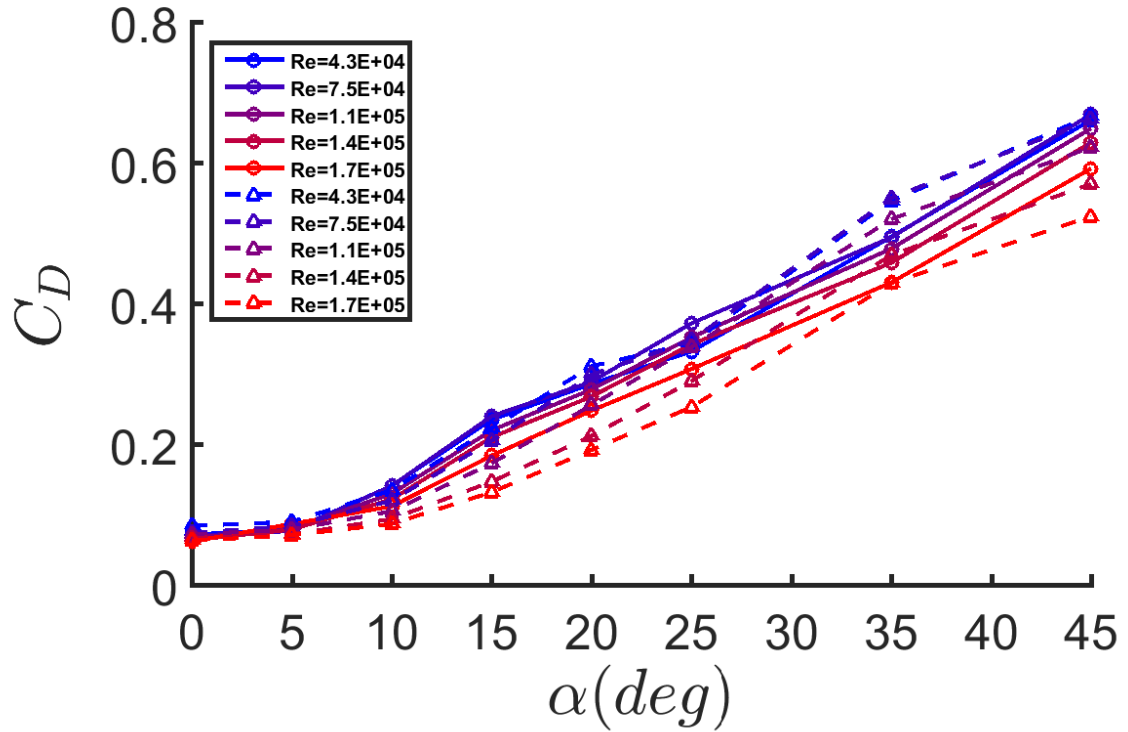
Figure 9: C_D as a function of α comparison of five-section continuous and separating wings

Figure 9 shows that the drag coefficient closely resembles the quadratic curve seen in typical airfoil drag plots. From $5° < \alpha < 25°$, the separating wings have a lower drag coefficient, and in both arrangements, the increasing Reynolds number yields a lower drag coefficient. The drag coefficient always decreased with increasing Reynolds number in both cases. This could be a result of higher wind speeds producing a greater twisting force the wing sections and effectively reducing their angle of attack. The reduction of drag coefficient for the separating wing compared to the continuous wing from $10° < \alpha < 35°$ could also be the result of the separation between the wing sections, which becomes larger

with increased wind speed, allowing the free stream air to inject momentum into the boundary layer thereby reducing the separation and lowering the drag.
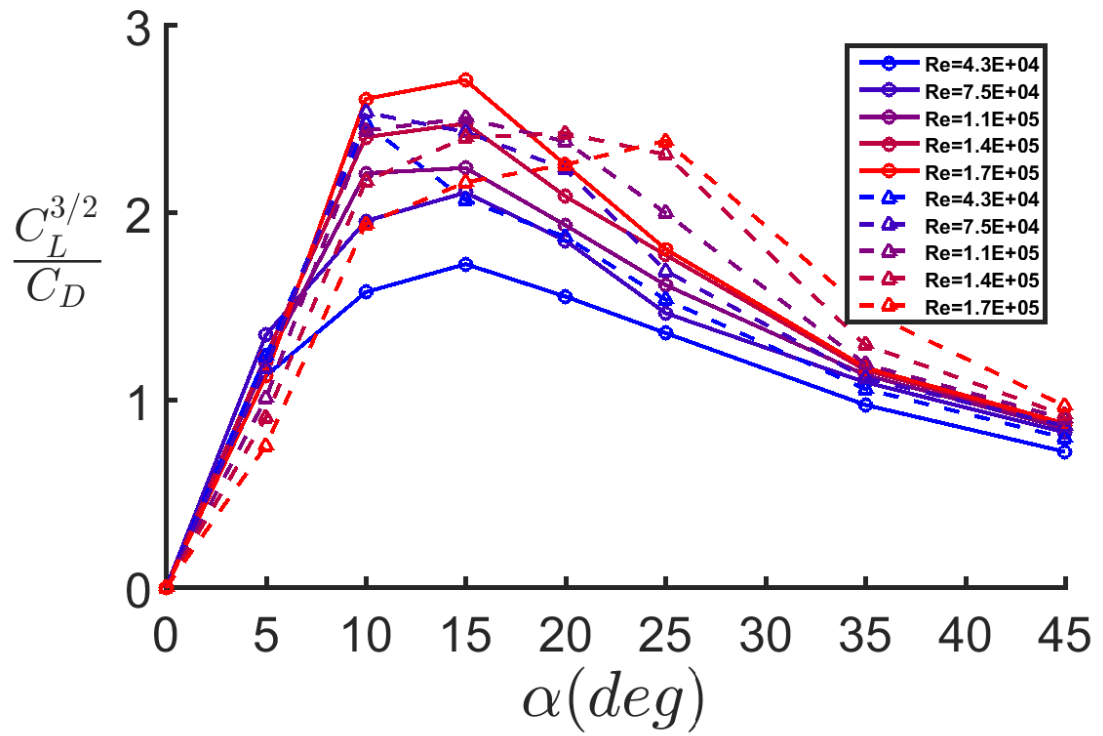
Figure 10: $C_L^{3/2}/C_D$ as a function of α comparison of five-section continuous and separating wings

Figure 10 shows that the continuous wing yields both the largest and smallest peak $C_L^{3/2}/C_D$ values. The values for the continuous wing increase with increasing Reynolds number, but always peak at $\alpha = 15°$. All $C_L^{3/2}/C_D$ values for a given Reynolds number for the continuous wing are greater than the values produced by all lower Reynolds numbers of the same wing type. Essentially the curves follow the same trend, but experience improved $C_L^{3/2}/C_D$ values with increasing Reynolds number. The separating wing, on the other hand, peaks at almost the same value for all wind speeds, but the peak values both decrease and occur at larger angles of attack as the Reynolds number increases. All the $C_L^{3/2}/C_D$ values are greater for the separating wing than the continuous wing for similar Reynolds numbers once $25° < \alpha$.
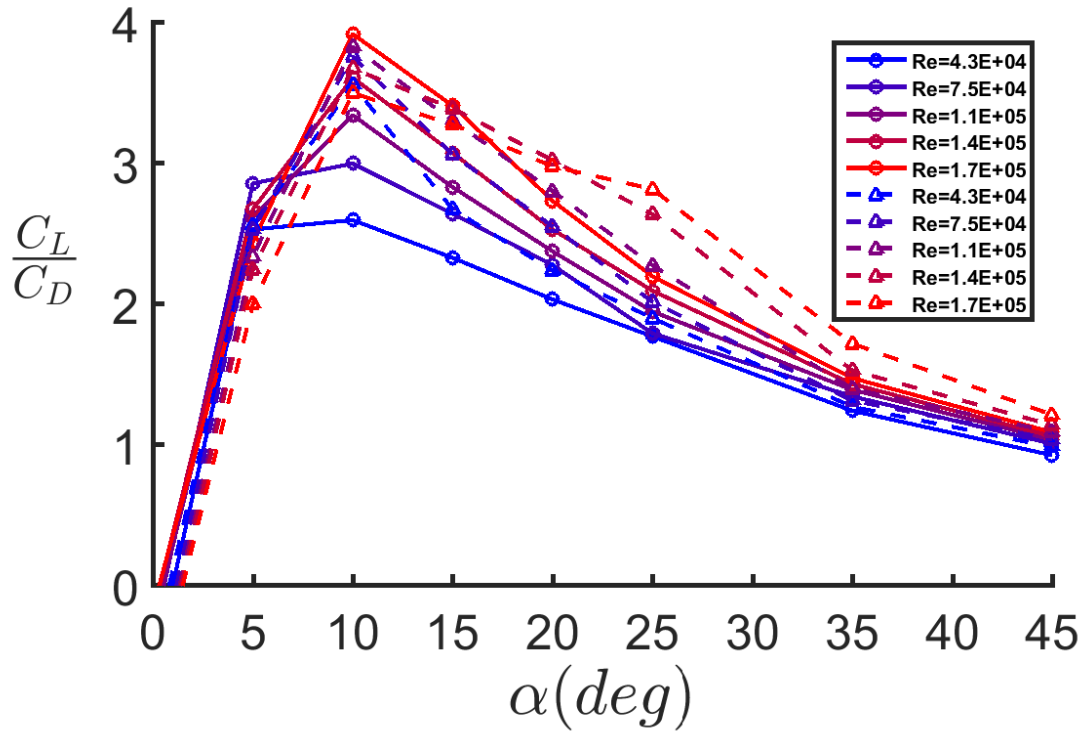
Figure 11: $\frac{C_L}{C_D}$ as a function of α comparison of five-section continuous and separating wings

Figure 11 shows that C_L/C_D reaches its maximum value at $\alpha = 10°$ for all Reynolds numbers in both configurations. The peak values of C_L/C_D increase from about 2.5 to nearly 4 as the Reynolds number increases while the separating wing has a C_L/C_D value that ranges from 3.4 to 3.8. From $10° < \alpha < 25°$ values decrease more rapidly for the higher wind speeds in the continuous wing case than the separating wing. This is readily apparent at $\alpha = 25°$. In fact, the values for the separating wing increase more slowly and fall more slowly than the continuous wing at the same Reynolds numbers.

Since the limiting factors for wing area are the length of the wing sections, which are determined by the length of the plane, and the sweep angle of the leading edge, there is not much that can be done to significantly increase wing area by moving these perimeter boundaries. However, an examination of the effect of sweep angle on the lift and drag coefficients would be worthwhile to examine in future work. In the current work, in the case where the wing sections separate, it would make sense that more sections could be added and the sweep angle of the leading edge could remain unchanged simply by increasing the overlap between wings. Once the wings are loaded in flight they would separate and the wing area would be increased without increasing the exterior dimensions. The separating wings showed improved peak lift coefficients compared to the continuous wings, so it makes sense to see if adding more wing area artificially increases the lift coefficient. This is exactly what was done in one of the tests with the half scale wind tunnel model; two wing sections were added to each wing. Data for the separating seven-section wing case was only taken up to an angle of attack of 25° since characteristics past this angle aren't applicable to typical flying conditions. The wing area used to calculate the lift and coefficients for the seven-wing section testing is the same value that was used in the five-section tests. In the following graphs the dashed line continue to represent five-section separating wings and the dotted line represents the new seven-section separating wings.
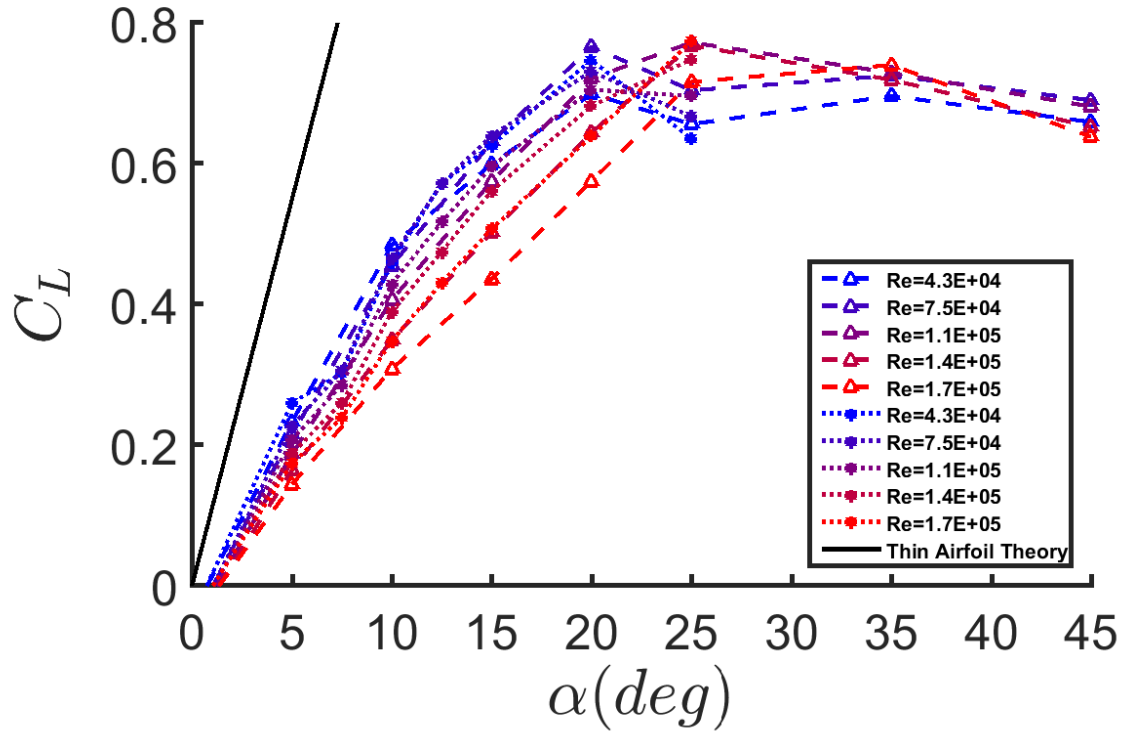
Figure 12: C_L as a function of α comparison of five and seven-section separating wings

The lift coefficient is slightly improved in Figure 12 when seven wing sections are used instead of five sections. With the exception of the data at $\alpha = 7.5°$, the seven sections produce a larger lift coefficient up to $\alpha = 15°$. This increase is most significant at the higher Reynolds numbers. With seven wing sections the trend of the lift coefficient dropping off later with increased Reynolds number is even more pronounced than the five wing sections. Unfortunately, data was only collected up to $\alpha = 25°$ so it is hard to know if the trend continues after that point.
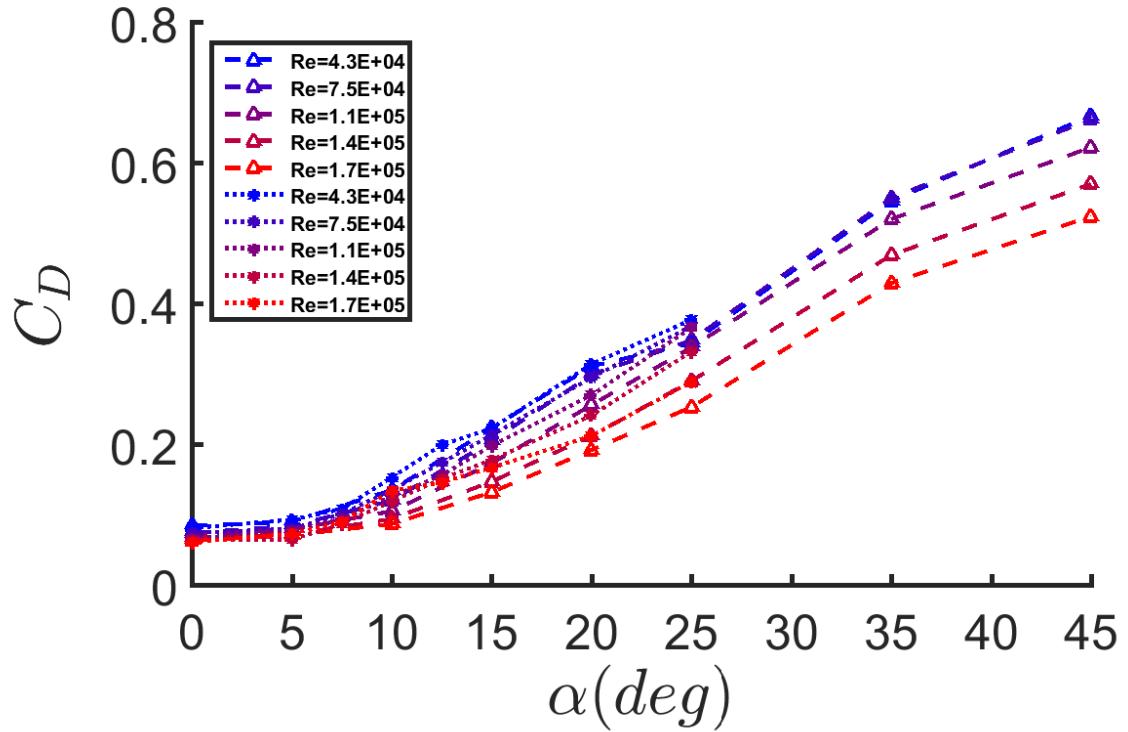
Figure 13: C_D as a function of α comparison of five and seven-section separating wings

Figure 13 shows that the coefficient of drag also increases when more wing sections are added. This becomes clear at $\alpha = 10°$ where the wing sections are beginning to separate and thus adding more obstruction to the air flow in the seven-section wing than in the five-section wing. The higher Reynolds numbers result in the largest percent increase in drag. At a Reynolds number of 1.7×10^5 the drag is increased by almost 100% and 50% at $\alpha = 10°$ and 15° respectively.
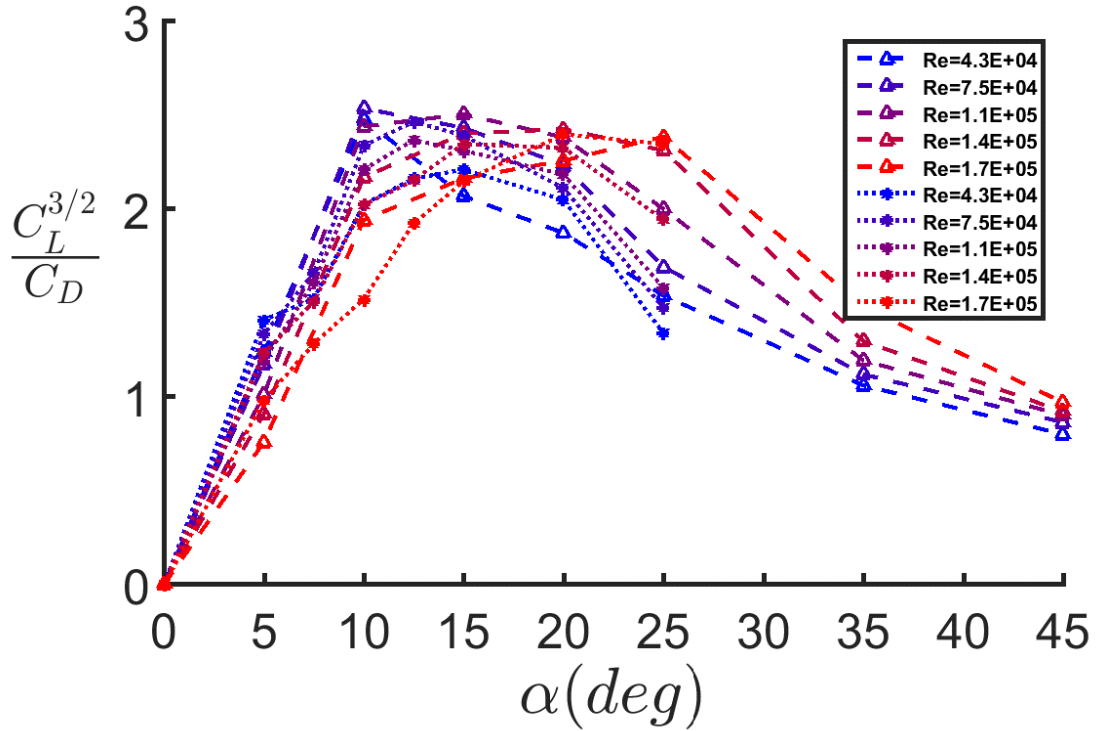
Figure 14: $C_L^{3/2}/C_D$ as a function of α comparison of five and seven-section separating wings

Figure 14 shows that the peak values of $C_L^{3/2}/C_D$ decrease with the added wing sections.

The peak values for the various Reynolds numbers are not similar to each other in the

seven-section case like they were with five-section case. In fact, there is not a clear trend

for the peak values of the seven-section. There is a large variation in $C_L^{3/2}/C_D$ values

throughout the Reynolds number range for both the five-section and seven-section wings

as the curves fall. This is very apparent at $25° < \alpha$.
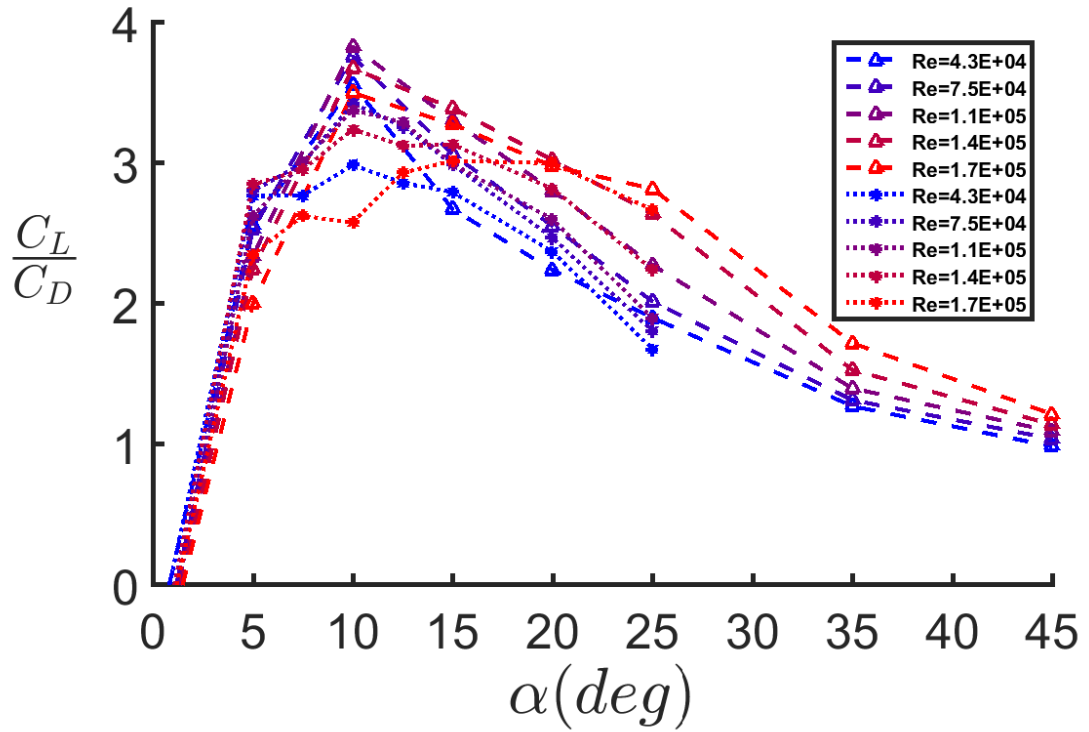
Figure 15: C_L/C_D as a function of α comparison of five and seven-section separating wings

The peak value of C_L/C_D decrease when wing sections are added. Figure 15 also shows the mid-range Reynolds numbers yield the largest peak values for the seven sections just like it does for five sections. This makes sense since the coefficient of drag increased by a larger percentage than the coefficient of lift when the additional wing sections were added.

3.2 Flight testing

The initial flight testing was conducted using a 3:1 scale model of the 40mm GLUAS made out of 0.2 inch insulation foam (see Figure 16). This initial model had the elevons on the second wing sections just like the 40mm model. The tail area was increased relative to the model to ensure that yaw stability was not an issue while tuning the other aspects of the model. The weight of this model was not scaled such that the wing loading and flight speeds did not directly correspond to the 40mm UAS. This both reduced the minimum flight speed and the wing loading. Flight could be maintained at just over half throttle where the model could be controlled with just the elevons which was one of the key aspects of this testing. At full throttle the entire trailing edge of the wing experienced an enormous amount of flutter. It was only flown in this state briefly and in a straight line as it looked close to failure and a rapid change in pitch very likely would have folded the wings. Figure 16 shows an early model before the elevons were moved to the third wing section (towards the tail). The new placement of the elevons improved the pitch performance at a slight decrease in roll performance. The main reason for this flight test was to validate that the planform shape was stable and could be controlled with elevons as the only control surfaces. It did this very well and justified continuing work on a UAS with this planform at its core.
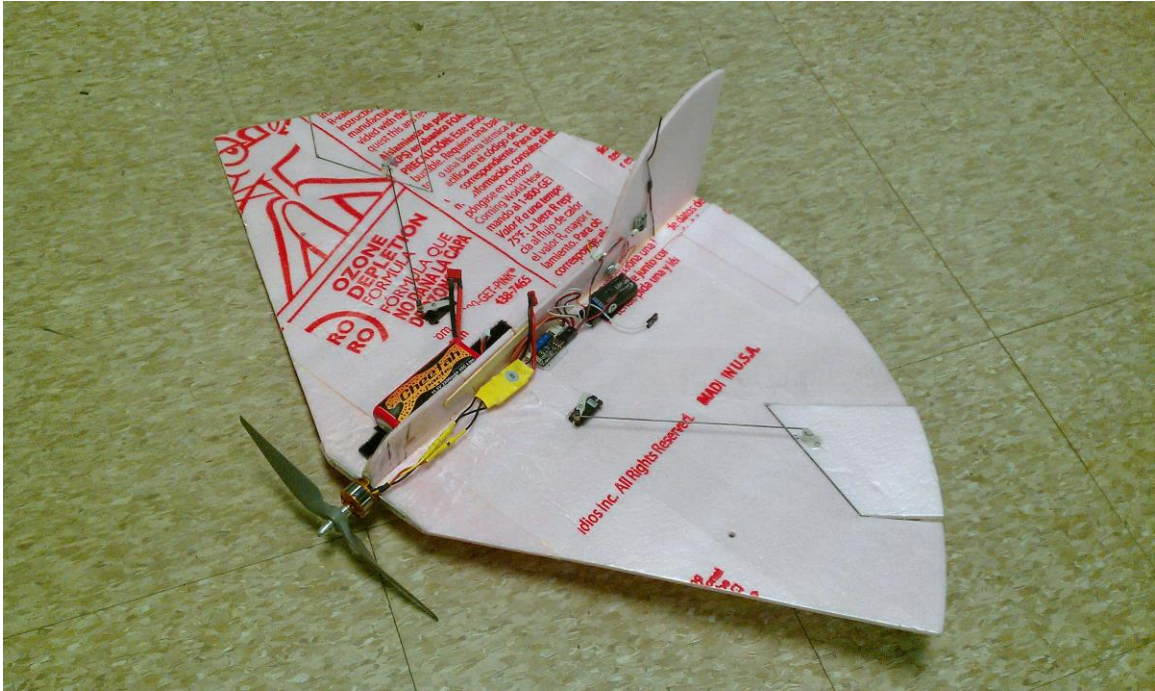
Figure 16: Test plane 3:1 scale of the 40mm model

4. Performance

4.1 Range and Endurance

For this project the prototype endurance requirements are 10-15 minutes and the range is 8-16 kilometers. Using Equation (1) and (2), the range and endurance are calculated for the GLUAS. These calculations are an iterative process based on the initial guess made for flight speed and data collected from the wind tunnel testing at that specific speed. Once a

battery weight has been decided upon the wind tunnel data is scanned for the maximum values of $C_L^{3/2}/C_D$ and C_L/C_D these values are used in the calculations.

	Range	Endurance
C_L	0.349	0.575
C_D	0.095	0.174
$C_L^{3/2}/C_D$		2.506
C_L/C_D	3.670	
E_{batt} (kJ/kg)	539	539
m_{batt}(g)	63	63
$W_{structural}$ (g)	286	286
S (m²)	0.097	0.097
ρ (kg/m³)	1.225	1.225
μ (Pa*s)	1.789×10^{-5}	1.789×10^{-5}
η	0.4	0.4

Table 1: Input Values for Range and Endurance Calculations from Model 4

Because the two values happen at different angles of attack, they yield different flying speeds for the best range and endurance calculations. These flight speeds and resulting Reynolds numbers are calculated using:

$$V_\infty = \sqrt{\frac{2W_{total}}{\rho S C_L}} \qquad (9)$$

where $V\infty$ is the free stream velocity. This velocity is used in Equation (3) to calculate the

Reynolds number.

	Distance	Flight Time	Flight Velocity	Reynolds Number
Range	14.6km	18.9 minutes	12.9 m/s	2.6×10^5
Endurance	13.1km	21.8 minutes	10.0 m/s	1.8×10^5

Table 2: Range and Endurance

The graph below shows the effect of the ratio of battery mass to the total weight of the

UAV on both the range and endurance.
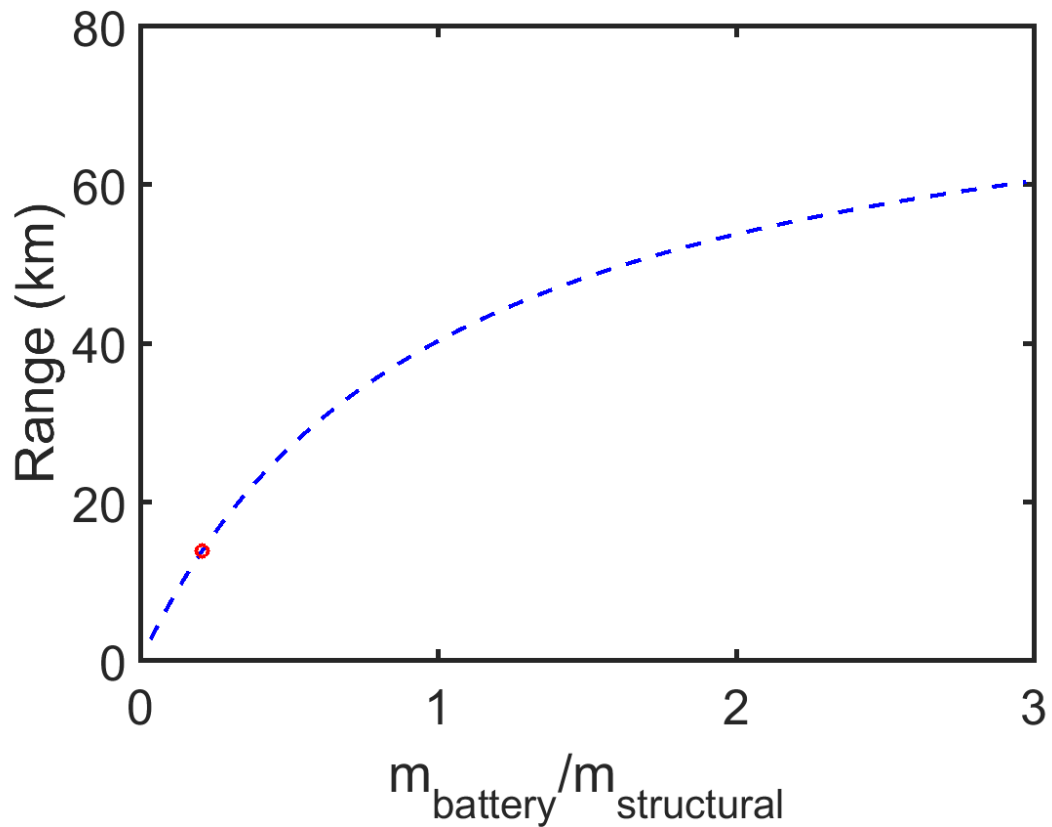
Figure 17: Battery mass as a function of range for constant structural weight

Increasing the battery mass relative to the structural weight will improve the range. Figure 17 shows that the battery mass chosen, and represented by the red circle, severely limits the range of the GLUAS. Additionally, this figure shows that as the weight of the battery approaches the total weight of the vehicle, the range approaches an asymptote just over 80 km.
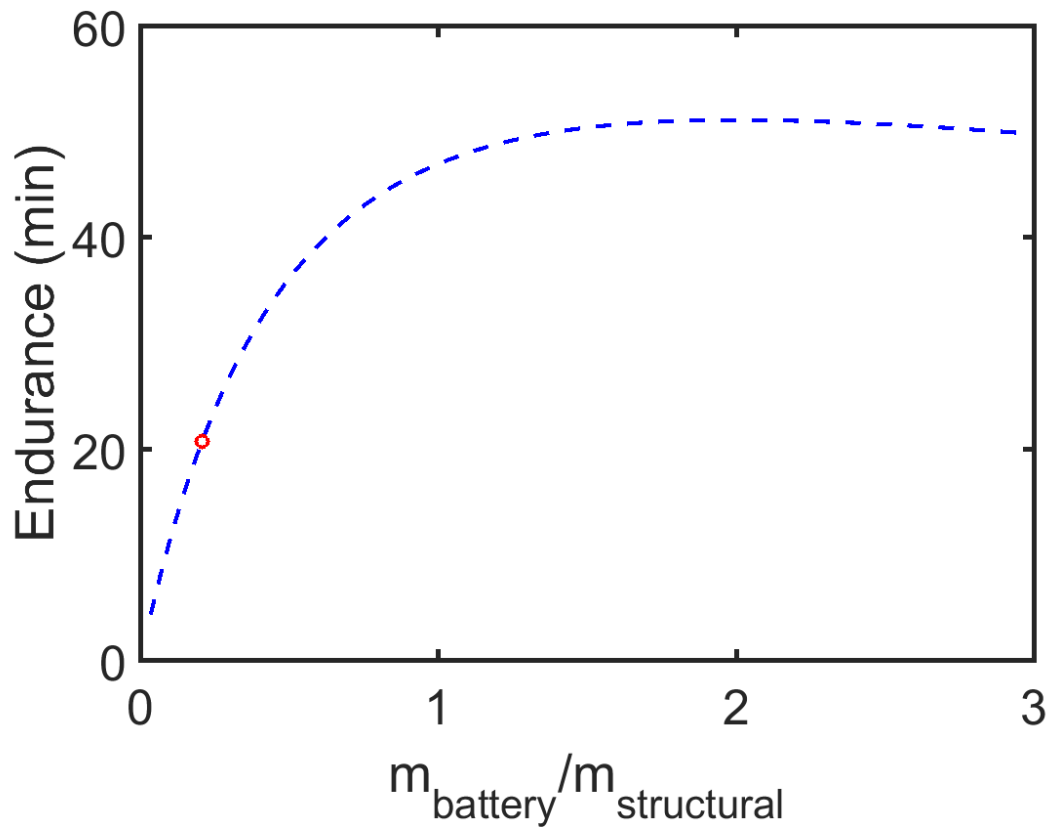
Figure 18: Battery mass as a function of endurance for constant structural weight

Figure 18 shows that endurance is maximized by having a battery that weighs twice the structural weight of the GLUAS, or 578 grams. Again, the red circle shows the endurance with the current battery.

Due to the high weight of the structure of the GLUAS and the fairly poor lift-to-drag ratio, it does not make sense to use such a large battery since that will require a much higher flight speed in order to generate the necessary lift.

4.2 Propulsion

The power system is composed of the battery, Cheetah 10A brushless ESC (electronic speed controller), 3-phase Cheetah A2204-14 brushless motor and the propeller. The battery utilized is a Cheetah 11.1 V 850 mAh lithium polymer (LiPo) battery which was selected based on the range and endurance requirements. The velocity ratio of the propeller wash to the free stream velocity is estimated to be 1.5 and the motor speed is specified to be 10000 RPM, which is half of the maximum motor speed. From this starting point the requirements of the components can be calculated using the following input values and the formulas:

	V_∞ (m/s)	$\tilde{V}$ (velocity ratio)	S (m²)	RPM	C_d (from data)
Range	12.9	1.5	0.097	1000	0.095
Endurance	10.0	1.5	0.097	1000	0.174

Table 3: Propeller Diameter and Pitch Input Values

$$T = \frac{1}{2}\rho V_\infty S C_D \qquad (10)$$

$$D_{Prop} = 2\sqrt{T/[\rho\pi(\tilde{V}V_\infty - V_\infty)^2]} \qquad (11)$$

$$\alpha_{Prop} = \tilde{V}V_\infty/(Rev/s) \qquad (12)$$

where T is the thrust, D_{Prop} is the propeller diameter, α_{Prop} is the pitch of the propeller and $\tilde{V}$ is the ratio of the propeller wash velocity to the free stream velocity.

The resulting propeller sizes are shown in the Table 4. The propeller that is used in the 60 mm GLUAS testing is an 8x4 inch propeller, or 203x101 mm. This number is very close to the calculated values and should be a good starting point for flight tests. It is also a very feasible size for packaging once a folding propeller is incorporated into the model.

	D_{Prop}	α_{Prop}	Thrust
Range	155 mm	104 mm	1.04 N
Endurance	208 mm	81 mm	0.93 N

Table 4: Calculated values for Propeller Diameter and Pitch

Additionally the propulsive efficiency can be calculated:

$$\eta_{propulsive} \approx \frac{2}{1+\tilde{V}} \qquad (13)$$

The resulting propulsive efficiency is 80%.

4.3 Control Surfaces

The only control surfaces on the GLUAS are the elevons which are located on the third wing section on each wing. Their placement is based on an initial guess as a compromise between the roll and pitch authority and then adjusted based on the flight tests of the foam model. Originally this model had the elevons on the second wing section which were

moved to the current location after testing. The control horn on the elevon is one of the reasons for using the wing section stacking order where the leading wing section is on top. This was the only means of mounting a control horn on the elevon that would not interfere with wing folding and be actuated from a servo fixed in the bottom half of the fuselage. If the stacking order were reversed, the servos would have to be in the top of the fuselage and the design does not have the space that would be required for this configuration.
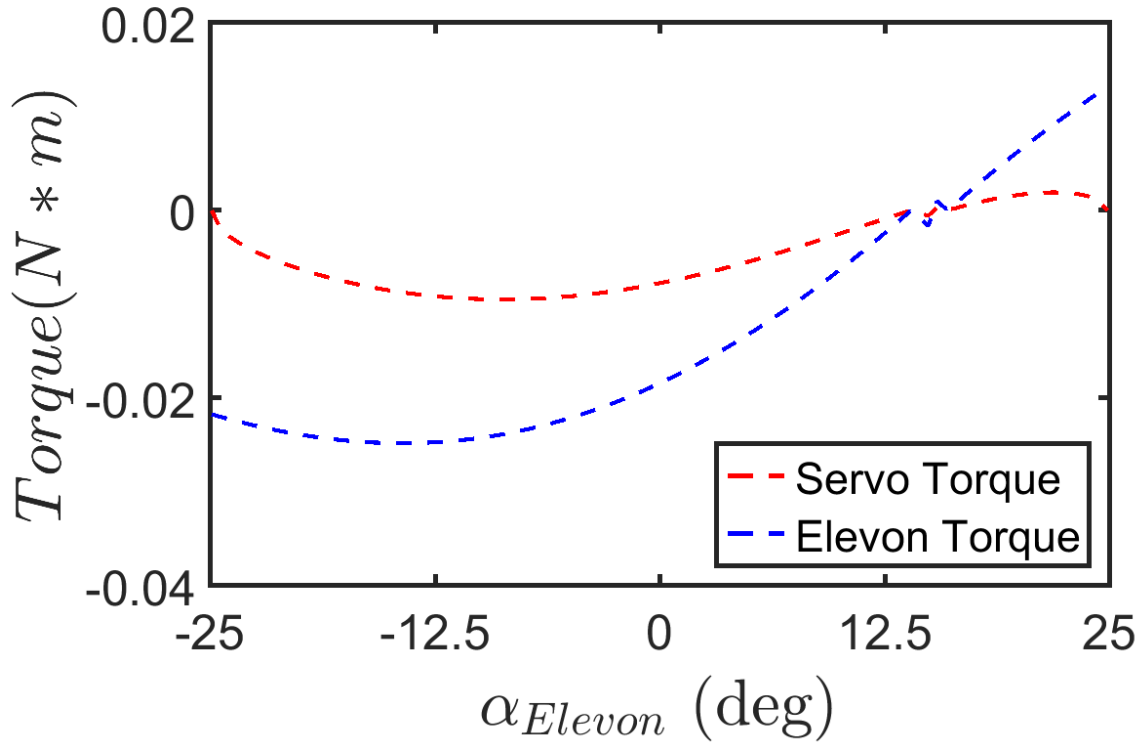
Figure 19: Elevon torque on servos as a function of elevon deflection angle relative to body

An ultra nano servo, is connected to the elevon control horn by a connecting rod. The ratio of servo arm to control horn is 1:2.38 which enables the servo to rotate 90° from rest when the elevon is deflected at 25°. This ratio provides both the advantage of reducing the required servo torque relative to the elevon holding torque and increasing the resolution of control over the position of the elevon. The result is a maximum torque of 0.01 Nm on the servo, which is obtained by using a HiTech HS-35HD that is rated to 0.078 Nm. Figure 19 shows the torque of the servo throughout the elevon deflection range. The forces exerted on the elevons were calculated using the lift and drag curves found when taking data for

41

the half scale wind tunnel model for the best range velocity as it is the higher of the two possible flight velocities and will result in higher forces on the elevons. The curve fitting of the wind tunnel data is the cause of the abnormal bumps in the torque at 15°. Deflection of the elevons is relative to the body of the GLUAS which is at an angle of attack $\alpha = 15°$. The attainable deflection of the elevon is about -20° to 20° due to interference of structural components preventing the servo from completing the full 180° of rotation.

5. System Level Design

5.1 Evolution of CAD Model

The development of the CAD model is an iterative process. Each component that is changed affects other aspects of the model, and so it is through many changes that the final design has been achieved. The starting point was the wings, control surfaces, and fuselage.

First a 40 mm model, Model1, was designed. It was composed of a 3D printed plastic fuselage and five wing sections per wing (Figure 20). The justification for five wing sections was the width of the fuselage; each wing section tip was the width of the fuselage requiring five wings to fill the planform. Each wing section was composed of a plastic root section and aluminum tip. The 3D printed plastic root had gears to mesh with the opposing wing and a latch system to hold spacing when the wing was open. The tip of the wing section was 0.4 mm thick. Figure 20 shows a complete left wing composed of five 3D

printed plastic root sections and five aluminum wing tips. The right wing is only shown as the root sections.
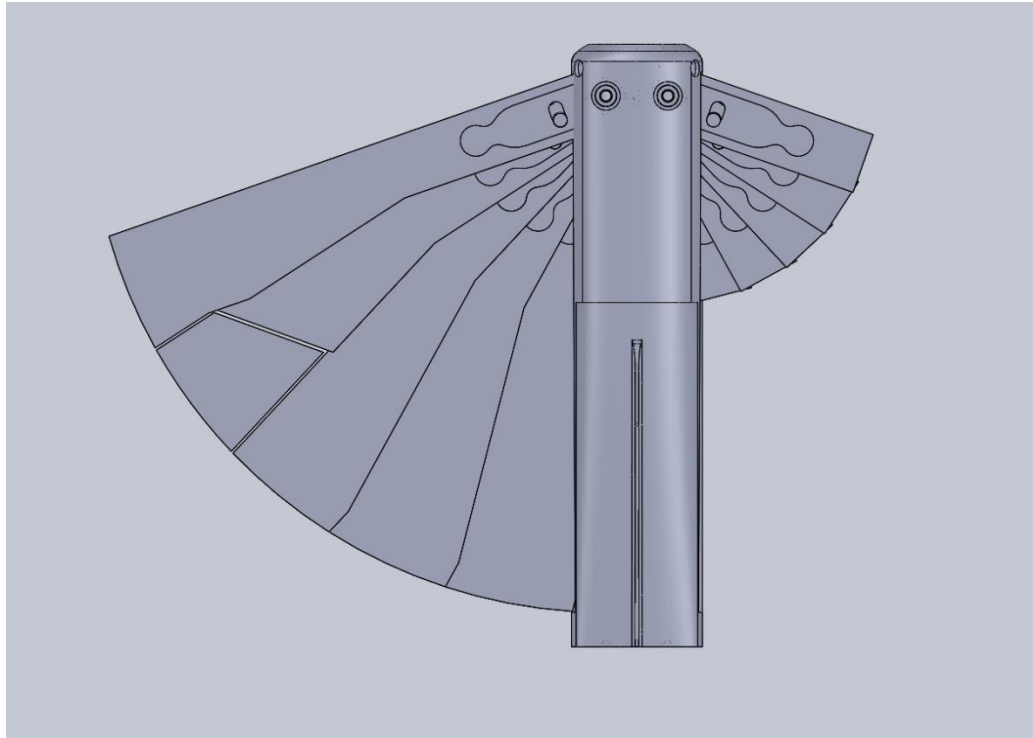
Figure 20: 40mm UAV Showing Wing Sections

In Figure 21, the first root section is highlighted in blue. In this image it is possible to see the meshing gear on the left and right sections and the catch mechanism that is used to pull the wings open. At the pivot point of each wing there is a pivot arm which fits into the leading wing section. It is used to open a wing via a linear spring (not pictured) acting on the arm.
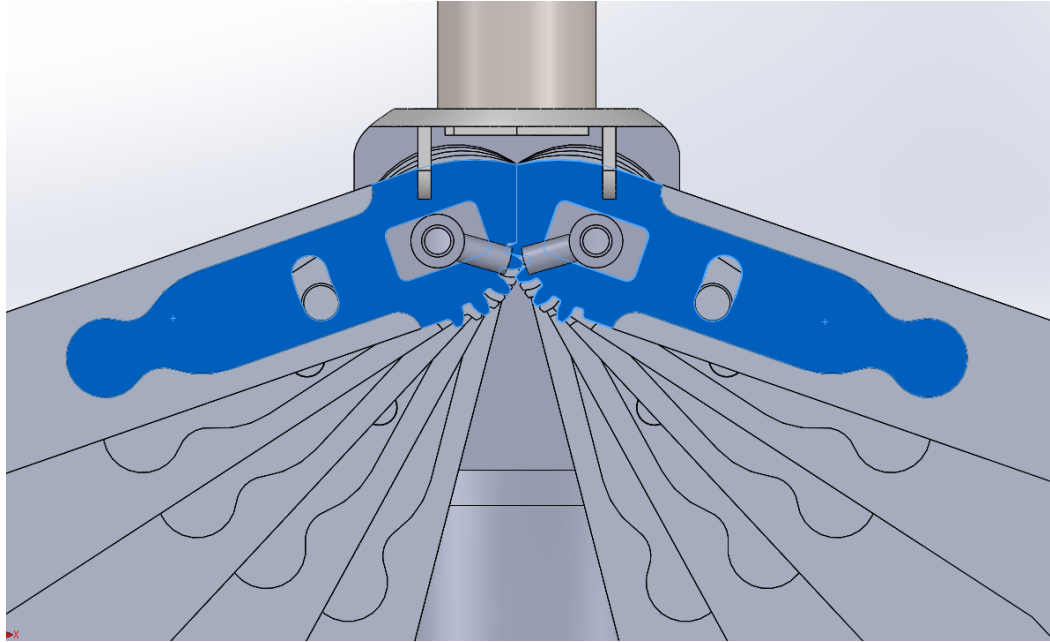
Figure 21: Geared Wing Sections and Catch Mechanism

 The second wing section from the leading edge is where the elevon is located. Aside from a folding vertical stabilizer on the bottom of the fuselage and a mount on the nose of the GLUAS for the motor, this model is designed with the placement of the electronics and method of elevon actuation undetermined. An important aspect of this design is that the wings are stacked from the mid plain of the fuselage upwards. This leaves the bottom half of the fuselage with more space to package the internal components including the battery and servos. The model of the full GLUAS is pictured in Figure 22. This initial model laid the groundwork for the wind tunnel models and the 3:1 scale foam test flight models.
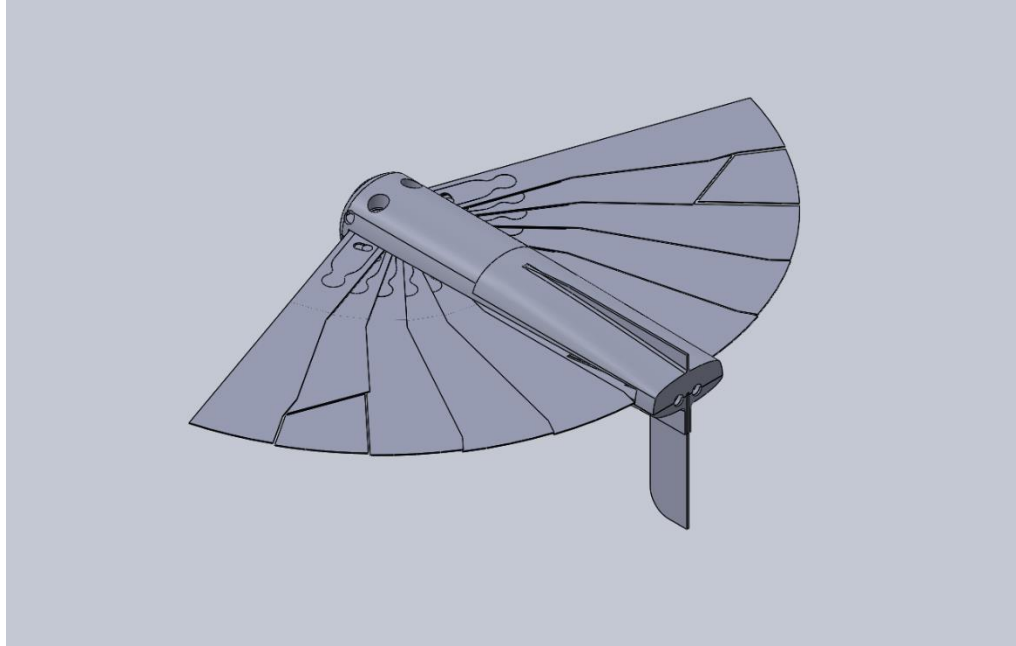
Figure 22: 40mm UAV with Tail Deployed

The second model, Model2, was essentially the enlargement of the 40mm model to 60mm. There was consideration to use a thrust vector control (TVC) pusher propeller configuration to eliminate the need for elevons and an actuation method for the elevons, but this idea was discarded as it added complexity to the controllability of the GLUAS and moved the CG significantly rearwards potentially making the GLUAS unstable. Also, it would most likely require a contra-rotating propeller to control roll, which increases the weight and complexity by adding a second set of folding propellers. Model 2 also featured a fuselage that fully enclosed the wings when they are closed just like Model 1. Figure 23 shows a side view of the model with wings in the open position. Only two bolts held the whole assembly together and doubled as the pivot point for the wings. The hole for the left wing bolt is visible on the top of the fuselage.
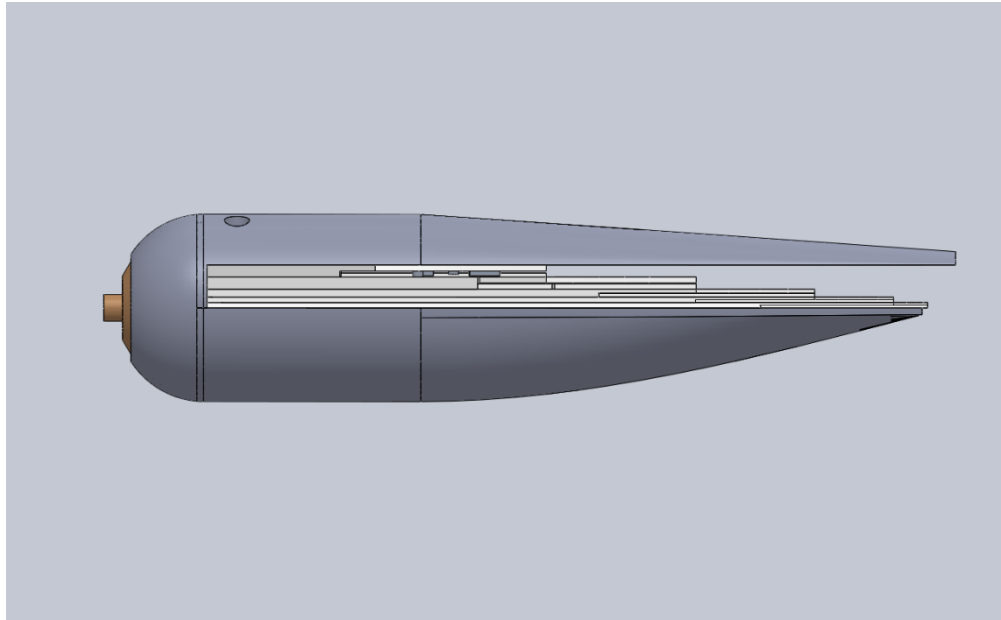
Figure 23: Profile of Model2

A top view of the GLUAS is pictured in Figure 24. The geometry of the right wing was mirrored and inverted for the left wing so the wing sections could stack neatly when they were folded closed.
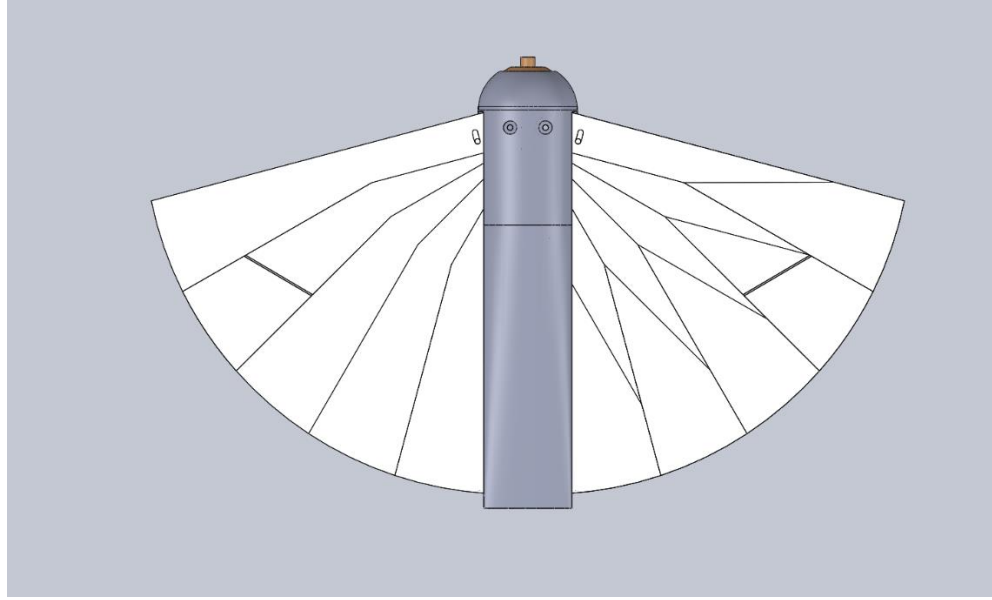
Figure 24: Model2 showing wing structure

Model3 was a continuation of the second model. The wings and elevons were extended past the end of the fuselage. This was made possible because the back portion of the fuselage no longer needed to be structural since the launch forces would be applied to the wing pivot bolt region and not to the tail of the fuselage. The tapered shape at the end of each wing section allowed them to fit inside of the tail of the mortar. Keeping the length of the fuselage unchanged and extending the wing section length allowed the GLUAS to exceed the initial design constraints for length while still fitting the mortar maximum length. The extended wing sections can clearly be seen in Figure 25. They lengthening of the wing sections resulted in only a 9% increase in weight while increasing the planform area by 48%.
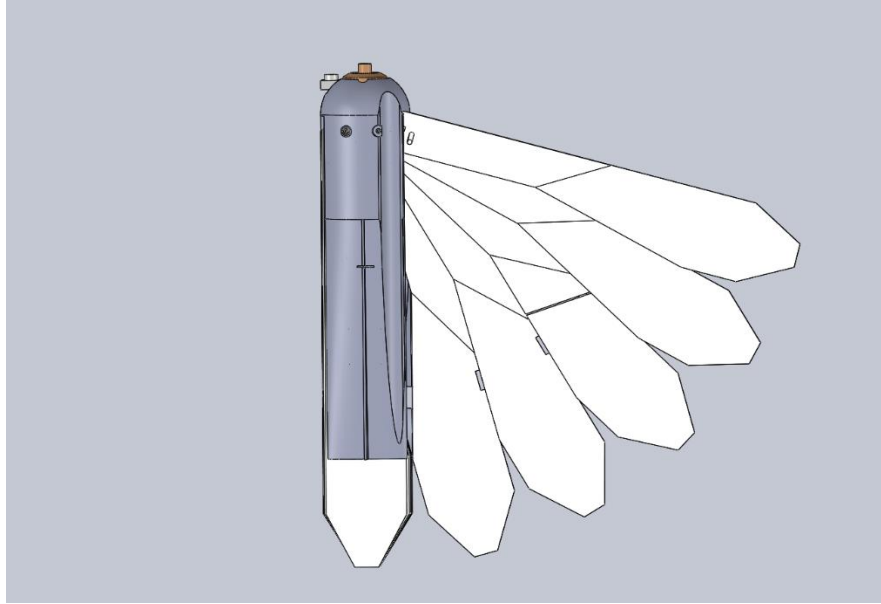
Figure 25: Model3 with extended wing sections
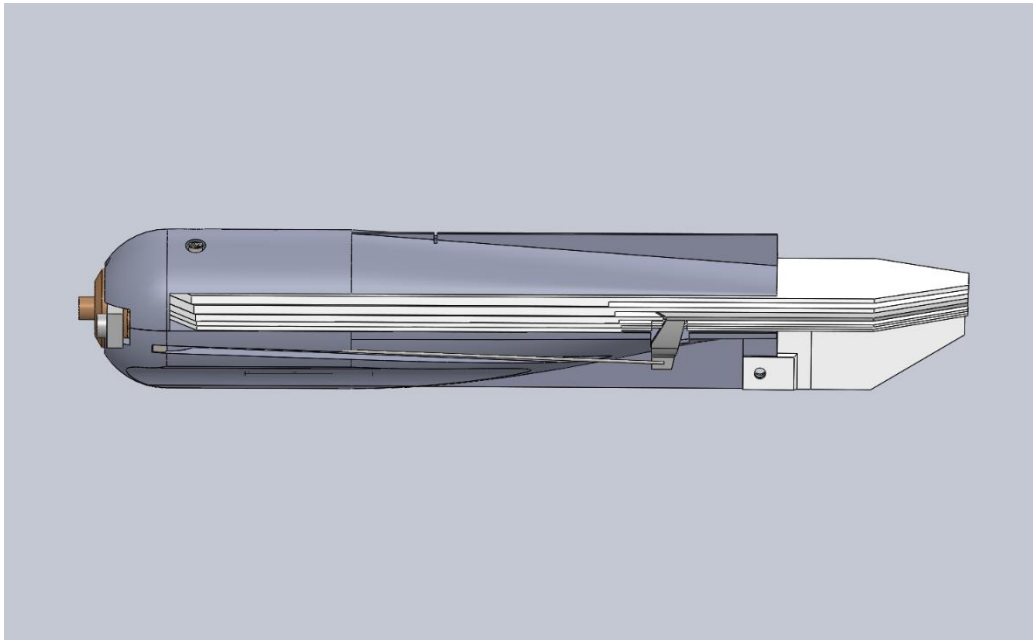
Figure 26: Profile of Model3 showing vertical stabilizer and collapsed wings

The vertical stabilizer also was supported off the back of the fuselage and extended back as far as the tips of the wings, see Figure 26. A folding mechanism was not decided upon for the tail, but a small spring or elastic strap would easily produce the 90° opening angle. This model also included space for two servo motors in the front of the fuselage and grooves that run the majority of the length of the fuselage to house the elevon control rods. The control rods and elevon control horns are shown in Figure 27. Additionally, one of the two recesses for the folding propeller can be seen on the bottom of the fuselage.
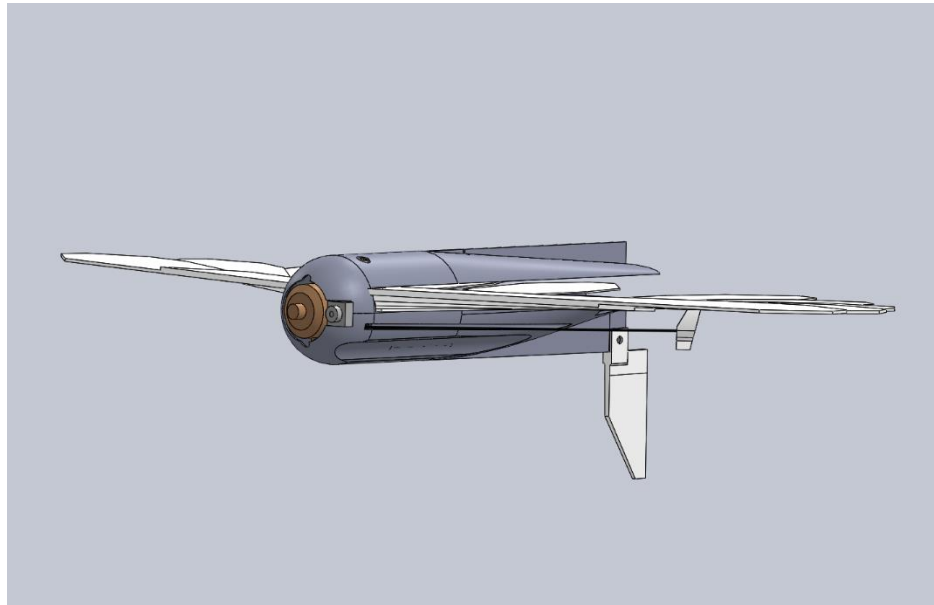
Figure 27: Open wings with elevon horns and control rods

A cut view of the front of the GLUAS shows the placement of the servos on the bottom half of the fuselage. The packaging was very tight and the recesses for the connecting rods occupied a large portion of the interior space of the fuselage. On the top half of the fuselage

the torsional springs were held in place by the wing pivot bosses and fit into a grove on the leading wing section to hold the wings open. These two features are evident in Figure 28.
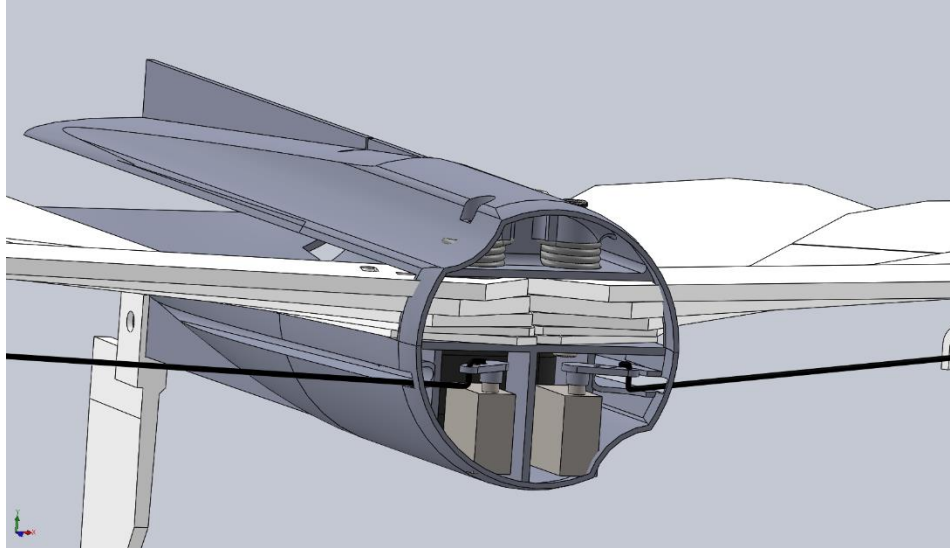
Figure 28: Cut view of servos and torsional springs

The electronics with the exception of the main battery were packaged in the top half of the fuselage with only the main battery and servos in the bottom. The electronics are shown in Figure 29. A notable feature is the addition of a second battery to power the autopilot in the hopes of avoiding brown out conditions when the servos are under high load.
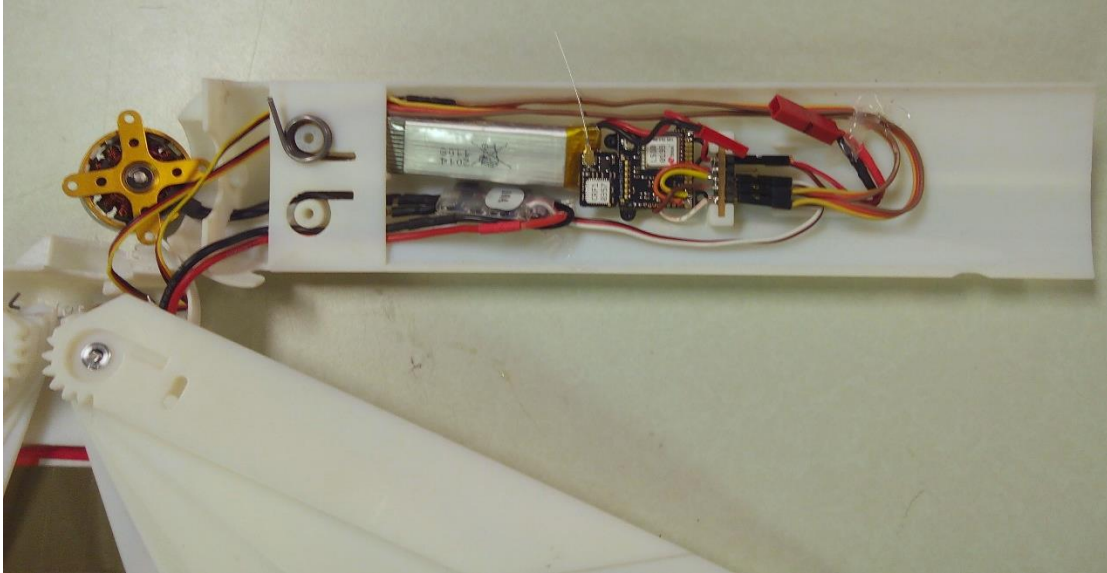
Figure 29: Electrical components in the top half of Model3

This model was 3D printed out of a resin based polymer and fitted with all of the electronics except the video system. There have been no flight tests with this model since it lacks first person view (FPV) capabilities and the resin structure was far too brittle to be a good test bed, but the control surfaces were actuated and moved without interference. Another important aspect was that the wings could not be printed hollow with this printer resulting in a model that was heavier than expected. Figure 30 is the fully assembled model powered on. Packaging tape was employed to act as the elevon hinges for this initial demo.
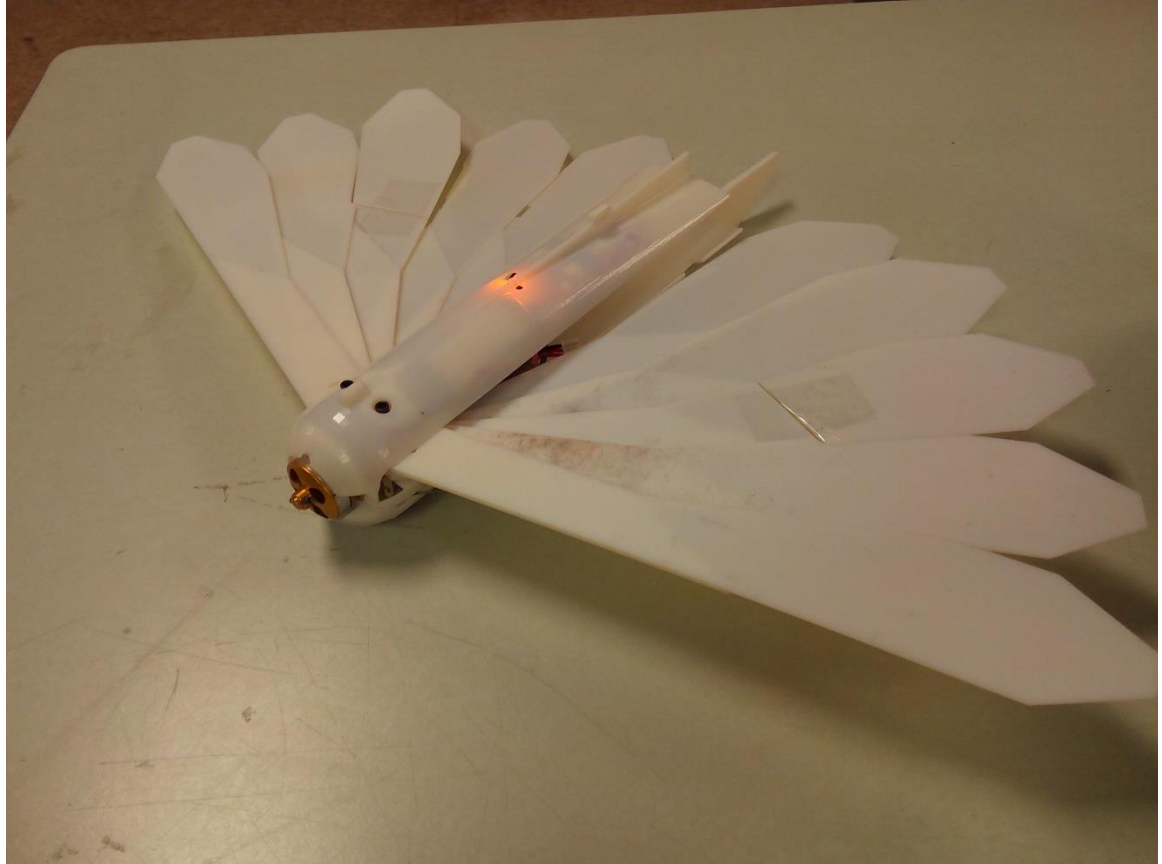
Figure 30: Model3 assembled

The major changes from Model3 to the current model, Model4, are that the electronics have all been moved to the bottom half of the fuselage. This makes assembly much easier by eliminating wires passing between the halves. The servos are inverted in Figure 31, so that the mounting points for the elevon control rods on the servo arms are closer to the bottom of the fuselage. In addition to making assembly much easier, this reconfiguration increases servo accessibility for changing servo arm lengths. Since the fuselage is narrower near the bottom, the recesses to fit the rods protrude to a lesser extent into the interior of the fuselage and there is more space to package the other components.
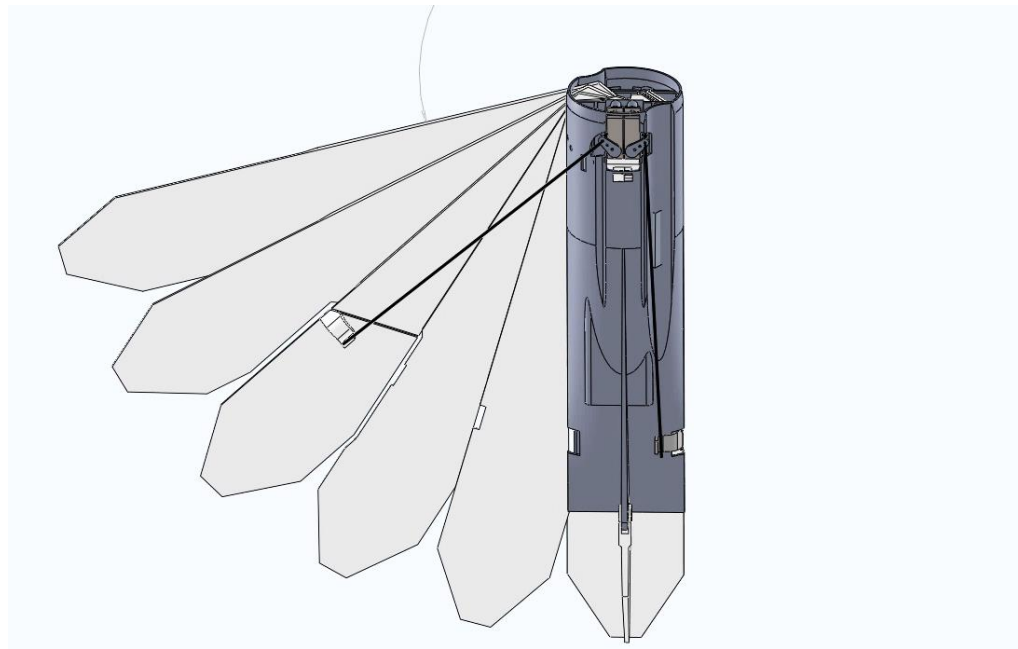
Figure 31: Model4 with inverted servos and new connecting rod placement

The final design is shown in Figure 32 and Figure 33. Two models have been built. Both

have hollow wings and full electronic packages including FPV video capabilities.
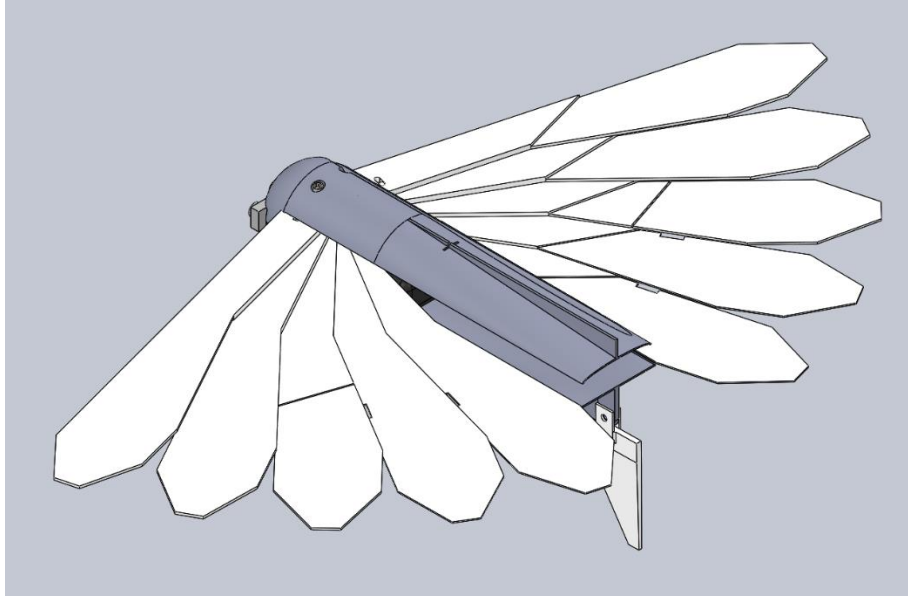
Figure 32: Model4 with wings and tail deployed
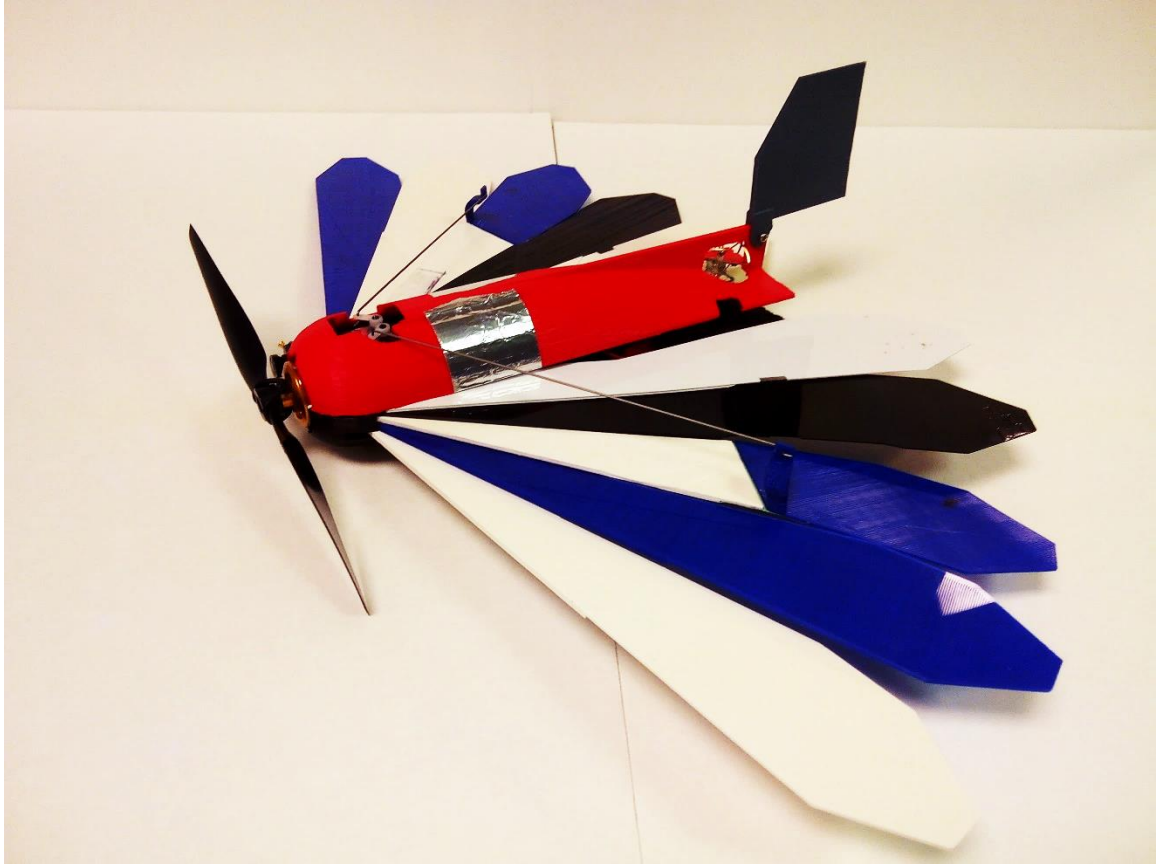
Figure 33: Assembled Model4 ready to fly (model inverted in picture)

	W_{total} (g)	L (m)	b (m)	S (m²)	AR	S_{elevon} (ea)	S_{elevon}/S	W_{total}/S (kg/m²)
Model1	280	.175	.307	.0335	2.8	.0010	.060	8.36
Model2	320	.245	.426	.0655	2.8	.0025	.076	4.89
Model3	349	.308	.545	.097	3.1	.0054	.111	3.60
Model4	349	.308	.545	.097	3.1	.0054	.111	3.60
Foam model	373	.425	.766	.198	2.9	.0125	.063	1.88

Table 5: Comparison of Models

Table 5 shows a comparison of the physical properties of the different models. The aspect ratio is roughly 3 for all of the models. Another important characteristic is that the increase in wing section length, b, from Model2 to Model3 resulted in a larger elevon to wing ratio and a large reduction in wing loading which is expected to improve controllability of the UAV. Also, L, the total length of the GLUAS with the wings closed has increased from Model2 to Model3

5.2 Physical Properties of Model4

The planform area, including the fuselage is 0.097 m². Using the following set of equations, the aerodynamic center of Model4 was calculated to be 79.5 from the leading edge of the wing.

$$S = \int_{-b/2}^{b/2} c\,\mathrm{d}y \tag{14}$$

$$MAC = \frac{1}{S}\int_S c\,\mathrm{d}S = \frac{1}{S}\int_{-b/2}^{b/2} c^2\,\mathrm{d}y \tag{15}$$

$$x_{cg} = \frac{1}{S}\int_{-b/2}^{b/2}(x_{LE} - c/2)c\,\mathrm{d}y \tag{16}$$

$$x_{AC} = x_{cg} + \frac{1}{4}MAC \qquad\qquad [20]\ (17)$$

During flight tests of the 3:1 scale of Model1 (2:1 scale of Modesl2-4), the aerodynamic center was located at 138 mm from the leading edge. From flight tests, the GLUAS was the most stable when the center of gravity was at 152 mm from the leading edge. This placement seems contradictory because the center of gravity (CG) is behind the calculated aerodynamic center, which, would make the GLUAS unstable. These calculations work best for rectangular wings, so it is to be expected that there will be some error for this wing shape. Taking the ratio of the aerodynamic center location to CG location from the foam model, a reasonable guess can be made for the design target of the CG of the GLUAS.

$$CG_{UAS} = \frac{CG_{foam}}{AC_{foam}} AC_{UAS} = \frac{152}{138} * 79.5 = 87.5mm\ from\ LE \qquad (18)$$

The components of the CAD model were designed to have a the CG at 87.5 mm from the leading edge, but the actual CG can be adjusted by about 10mm forward or back just by moving the battery forward or backwards.

In the final design, the wings vary in thickness. On all of the wing sections the root is thicker than the tip and it has a smaller width than the tip. These features exist partially due to packaging constraints and partially to minimize bending deflections caused by the aerodynamic forces. The root portion of the wing sections for the left and right wing fold into the fuselage side-by-side such that their width is limited to half the diameter of the fuselage. Further down the length of the wing section, the left and right wing sections begin to overlap. This makes it necessary for the tip regions of the wing sections to be half as thick as the root since there are twice as many wing sections stacked into the same space. Due to the fact that the wing tips do not see the same bending moment as the root, they can be made half as thick to fit the space constraints while still maintaining a sufficient factor of safety to not fail under load. The wing overlap is shown with two wing sections in Figure 34. At the root of the wing sections the top and bottom surfaces share the same plans, and about half way to the tip they are reduced to half their original thickness and offset from each other.

Figure 34: Overlapping wing sections for packaging

In addition to a reduction of thickness from the root to tip of the wing sections, they also

vary in thickness from one to the next. The specific thickness values are shown in Table 6.

These values are a result of the wind tunnel testing. In testing, it could be seen that the

leading wing sections deflected the most and there was very little motion in the trailing

sections. The wind tunnel used a model with aluminum wings, so the wing thicknesses

were scaled for the larger model and the change in the modulus of elasticity when plastic

is used in place of aluminum using Equation (8).

	Root Thickness	Tip Thickness
Section 1 (leading)	3.2 mm	1.6 mm
Section 2	3.2 mm	1.6 mm
Section 3	2.4 mm	1.2 mm
Section 4	1.6 mm	0.8 mm
Section 5	1.6 mm	0.8 mm

Table 6: Wing Section Thicknesses

While a pusher propeller on a gimbal for TVC was briefly considered, it made the most sense to use a tractor propeller set up for packaging and to keep the CG from moving aft. A statically stable plane is much easier to fly initially than a plane with thrust vectoring and an un-tuned controller. Additionally, the motor in the front maximized the length of the wing sections, which in turn maximized the wing area and minimized the necessary flight speed. Finally, having the motor up front keeps the weight close to the wing pivot bolts where the forces from the mortar shell will be applied when the GLUAS is launched. This means that the tail portion of the plane does not need to be reinforced to be load bearing resulting in weight savings.

Fully equipped, the GLUAS has a total weight of 349 grams. Weight of the electrical components make up only a small percent of the weight of the GLUAS with most of the

weight coming from the wings and fuselage. This is unavoidable when the components are made out of 3D printed plastic and the GLUAS is designed to have such a large wing area while still meeting the customer specified constraints.

5.3 Wing Folding Mechanism

Packaging is a critically important and very difficult aspect of this project. The most difficult components to package were the folding wings, the wing opening mechanisms and the elevon activation mechanism. The electronics also required careful placement, but their placement was less critical than the moving parts. Since these parts did not have rigid requirements for their physical placement like the moving parts, their placement became more about accessibility and their effect on the CG of the GLUAS.

The wings pivot around two bosses near the front of the GLUAS. The screws passing through these bosses hold the wings in place and are the main structure holding the top and bottom halves of the fuselage together. The leading wing section of each wing is connected to a torsional spring mounted in the top half of the fuselage. These springs provide the force necessary to deploy the wings. Additionally, the left and right wings have gears that are centered on the pivot axis that mesh together in order to open the wings evenly. In order to open the remaining wing sections, there is a boss and groove in each wing section. The boss slides within the groove of the previous wing section, such that as the leading wing opens it catches the boss on the next wing and, one by one, each section is pulled into the open position. The positions of the bosses are staggered from on section to the next to allow

the smooth opening of the wings. On the right wing, the bosses are located on the top surface of the sections and the step down to the tip thickness occurs on the top surface. The left wing has both the boss and step down occurring on the bottom surface. This reversal allows the wing tips to mesh together when the wings are closed.

The values for the torque required to hold the wings open are easily calculated using the flight velocities and coefficients of drag for both the maximal endurance and range flight conditions.

$$Drag = \int_{y_{root}}^{y_{tip}} \frac{1}{2} \rho V_\infty^2 C_D ([x_{LE}(y) - x_{TE}(y)]) \, y \, dy \qquad (19)$$

The resulting torque is 0.04 N-m per wing in the case of maximal range and 0.045 N-m per wing in the case of maximal endurance. The springs used are 120° torsional springs which exert a torque of 0.4 N-m when fully compressed. The wings open to a sweep angle of 15° meaning that, in the open wing position, the springs will exert a torque of 0.116Nm each since they are compressed to 35°. This is over 2.5 times the values that are calculated for either the maximal range or endurance flight speeds and drag values.

5.4 Elevon Control Mechanism

The two elevons make up about 11% of the total wing area. Ideally, for performance, the elevon pivot axis should be perpendicular to the air-flow, but due to packaging constraints it is easier to have the pivot axis perpendicular to the length of the wing sections. The final design is a compromise between these two conditions. The control horn is mounted to the leading edge of the elevon and points downward so that it can clear the other wings when they are folded away. Furthermore, the horns are bent such that they fit within the required circular profile of the fuselage. Metal rods connect the elevon control horns to the servos. Figure 35 shows the relation of the servo, connecting rod and elevon horn as they would be assembled in Model4. The mounting point on the servo arm lays on the wing pivot axis. This keeps the elevons in their flat, neutral position throughout the opening of the wings since the distance between the servo horn and elevon pivoting axis remains constant. The ratio of elevon control horn to servo arm is very important. This ratio determines both the throw of the elevon and the torque required by the servo to move the elevon under aerodynamic loads. Ultimately, the servo will rotate through as much travel as possible while still being able to move the elevon through the required angles to maintain the highest torque and control resolution possible.
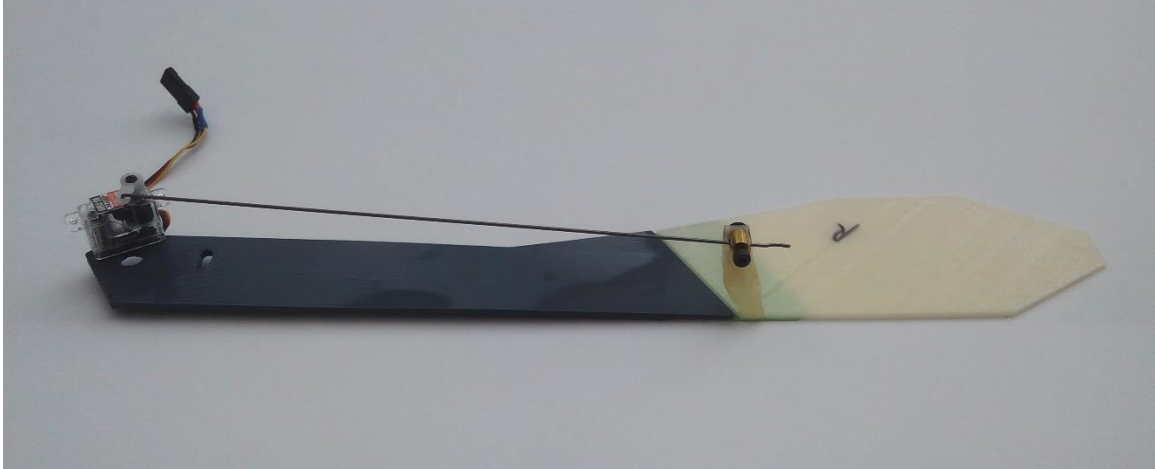
Figure 35: Elevon with connecting rod and servo

A folding propeller is not currently in the model or on the tested prototype, but will be required for a more complete prototype that can be gun launched. This design will require packaging the propeller in such a way that it will not interfere with the folded wings and other internal components.

5.5 Power and Video Systems

The bottom half of the fuselage houses all of the electrical components. One battery is used for all of the electrical needs. There are two circuits run off of the battery. The first circuit is powered by the electronic sped controller ESC and includes the two servos, the camera, the video transmitter and the motor. The second circuit is composed of a 5 volt battery elimination circuit (BEC) and the autopilot. This is on its own circuit to avoid born out situations which would crash the autopilot.

The objective of this project is facilitate high quality video of battlefields and surrounding terrain. To this end, video quality is very important. Because the autopilot receiver operates on 2.4 GHz, the remaining frequencies commonly available to the hobbyists are 900 MHz, 1.2 GHz and 5.8 GHz. 1.2 GHz is not recommended since it is half of the frequency of the receiver which can result in interference problems. While the lower frequency of the 900MHz will penetrate physical obstructions better than high frequencies, ultimately 5.8G Hz was chosen as it will return higher quality video.

The on-board components of the video system consist of a 700TVL NTSC camera with a 170° lense, 200 mW video transmitter and a 5.8 GHz ImmersionRC clover leaf antenna. The camera was mounted on the nose of the GLUAS for FPV flight since the 60 mm 3D printed plane is too small and fast to easily fly third-person view (FPV) from the ground. Later, the camera will be moved to point downwards for surveillance and the plane will be flown autonomously. If there is a need for a forward facing camera a second one can easily be added. The electrical components and their placement in the bottom half of the fuselage can be seen in Figure 36.

Figure 36: Packaging of video and electrical power components

The ground station component makes up the second half of the video equipment. Again there is a clover-leaf antenna, but this time it is connected to a 5.8 GHz receiver. The output of the receiver passes to a mini digital video recorder (DVR) and FPV screen which are run in parallel to avoid latency issues. The ground station is powered off of a 12V lead-acid motorcycle battery to maintain portability. A waterproof case holds all of these components and the laptop computer that is used to communicate with the autopilot. This full assembly is pictured in Figure 37.

Figure 37: Ground Station

5.6 Guidance, Navigation and Control

The on-board controller is a 2 cm by 3 cm board called a Lisa/S. This autopilot runs Paparazzi UAV and incorporates GPS, a receiver, telemetry downlink, IMU, barometer, magnetometer and controller all in one small package. Not all of the features are currently used as it runs open source code from the Paparazzi UAV project and experiences bugs, but its many features will be useful to meet the requirements of the final deliverable to the customer. Currently the GLUAS is flown with the man-in-the-loop, so that it is easier to understand the characteristics of the plane and keep it airborne. Later flights will be autonomous.

6. Field Testing

6.1 Carrier Plane

A carrier plane was built to launch the UAS for the initial tests. This plane would take the GLUAS up to altitude before releasing it. The hope was that this procedure would avoid the rapid and catastrophic failures that can result from launching an unstable planform close to the ground. The carrier plane would give the pilot time to react and recover the GLUAS without the worry of being in close proximity to the ground. Figure 38 shows the GLUAS mounted to the six-foot wing span carrier ready to be flown. The GLUAS is held on to the Carrier plane by two rods connected to a servo. This allows the GLUAS to be released when the pilot is ready and is very simple to minimize issues.

6.2 60mm GLUAS Flights

The initial GLUAS flight was a hand launch because the carrier plane was broken in a test flight with the second pilot. Instead of the planned carrier drop, GLUAS was launched by a person on the ground with the throttle at close to full power. The pilot was connected to a pair of FPV goggles and was seeing through a camera mounted on the side of the GLUAS. The release was a moderate throw, at which point the GLUAS traveled 5 meters and promptly dove nose first into the ground. The motor mount on the plastic fuselage was broken and testing was called off until the carrier plane could be repaired.

The carrier plane was repaired in time for the second test flight. This time the GLUAS was mounted to its underside and released at approximately 50 meters above the ground on the pilots command. Initially, after release the GLUAS flew unpredictably and was unstable at ¾ throttle. About five seconds into the flight the prop saver holding the propeller onto the motor popped off and the propeller was lost. At this point the GLUAS became stable. Roll commands yielded a slight roll and some yaw, but there wasn't enough command to invert the GLUAS. This is probably due to the bending of the wing sections that created dihedral like what was seen in the wind tunnel. The GLUAS glided into some tall weeds and was recovered without any damage.

The third flight was also launched from the carrier plane. The prop saver on the GLUAS propeller was reinforced with some fishing line to keep it from coming free as in the

previous flight. This time the motor on the carrier plane broke its mounting and a rushed drop was required before the carrier plane lost altitude. Upon release, the throttle was pushed to wide open and the GLUAS started spinning about the yaw axis in a flat spin about the positive z-axis. No amount of throttle adjustment or motion of the elevons in either pitch or roll could get the GLUAS out of the spin. Once again it landed in tall weeds and was recovered intact. The initial thought was that the propeller on the loose motor on the carrier plane had damaged the GLUAS causing the yaw issue, but this was clearly not the case upon inspection on the ground it was determined that the GLUAS was not damaged before release.

A fourth launch was conducted. This time the GLUAS was unintentionally flipped into an inverted position under throttle immediately after launch. Again it went into a flat spin, only this time it was in the opposite direction relative to the ground. So it was still spinning around the positive z-axis in the reference frame of the GLUAS. This flight also ended in the weeds but this time one of the catch bosses on a wing section broke and the GLUAS was not in a condition where another flight made sense especially since it seemed that there was a yaw issue present that needed to be corrected before future flight would be beneficial.

At this point many hand launches were conducted with the wing section taped back into place. Under no power, the GLUAS would glide nicely, but anything above ¼ throttle would result in the GLUAS trying to roll and sharp yawing at which point it would crash.

6.3 Understanding of issues

The major challenge with achieving straight and level controlled flight seems to be the flat spin. It is hypothesized that this is due to the fact that the vertical tail is on the bottom of the GLUAS meaning that the propeller wash would hit it on the right side and in turn cause a positive yaw. This is supported by the fact that when the GLUAS was inverted in the fourth flight, it yawed to the left because now the tail was on the top of the fuselage. It is thought that at low speeds, occurring at launch, that there is not enough flow over the tail and wings so that the only force the GLUAS experiences on its flight surfaces is the side force on the tail. To correct this, future flights should dive nose down upon release and only turn up the throttle once a higher air speed is achieved, and the throttle should be increased slowly to limit and torque roll issues. A second option is to add a second tail on the top of the fuselage to balance the yaw force. A potential side effect could be that that any roll issues caused by the propeller wash on the tail would now be doubled and roll stability could become an issue.

7. Future Work

There are many facets of this project that will benefit from additional research, which will provide future enhancements to the design. The initial target was to get a UAS flying that met the minimum requirements specified in the original proposal, but after this is achieved

and the components of the UAS are understood there are many possibilities for improvement.

7.1 Carrier Launch/Gun Launch

A carrier plane has been built to launch the UAS for the initial tests. This plane will take the GLUAS up to altitude before releasing it. Hopefully this procedure will avoid the rapid and catastrophic failures that can result from launching an unstable planform close to the ground. The carrier plane will give the pilot time to react and recover the GLUAS without the worry of being in close proximity to the ground. Figure 38 shows the GLUAS mounted to the six foot wing span carrier ready to be flown.

Figure 38: UAV Mounted to Bottom of Carrier Plane

The research thus far has been a proof of concept that an airframe of this shape can fly and maintain the flight requirements described. The design has evolved with these requirements in mind paying extra attention to the physical constraints required to be packaged in the specified dimensions. The features of the design reflect the requirement that it be a robust structure, but the materials used at this point in time will not be able to handle the loads of a gun launch. Prior to a gun launch there should be a tube launch. This tube launch will fire

the GLUAS into the air from the ground with the wings tightly folded. When the GLAUS reaches peak altitude, probably in the 10-20 meter range, the wings will open, the prop will unfold and normal flight will be initiated. This step will prove that the GLUAS can deploy its wings without problem before investing the time and money in a more robust model for gun-launching.

7.2 Wind Tunnel PIV Testing

The GLUAS has not been tested with a particle image velocimetry (PIV) system up to this point. Future work should include characterizing the GLUAS using the PIV with both wing stacking configurations and different wing section thicknesses. This will help with understanding the force data from the wind tunnel and shed light on potential improvements. It would also be worthwhile to test a model with a powered propeller to examine the interaction of the wings and tail with the propeller wash. The current model is too large for the wind tunnel so either a larger tunnel will be needed or the GLUAS, motor and propeller will need to be scaled down to fit the current wind tunnel. In this design, the propeller wash covers the majority of the wings and all of the tail surface so these interactions are very important for design and controllability.

7.3 Morphing Wings

The next generation of the GLUAS will most likely incorporate morphing wings. This will start with a study of possible shapes and folding mechanisms. Actuation of the morphing control will most likely incorporate a device consisting of piezoelectric actuators. These morphing wings will be made of a thin membrane of either fabric or plastic to minimize packaging volume requirements and reduce wing weight. While morphing wings were not the focus of the first generation GLUAS they could provide many benefits in improving the aerodynamics and increasing its performance in future work.

8. References

[1] T. D. Casiez, "Compact, High-g, Efficient Folding Wing for a Cannon-Launched Reconnaissance Vehicle," Massachusetts Institute of Technology, 1998.

[2] D. R. S. M. A. S. A. A. Jonathon I. Henry, "Design, Construction, and Testing of a Folding-Wing, Tube-Launched Micro Air Vehicle," *43rd AIAA Aerospace Sciences Meeting and Exhibit,* 2005.

[3] C. Sudduth, "Design of a Hybrid Rocket/Inflatable Wing UAV," MS Thesis. Oklahoma State University, 2012. Web. 2016.

[4] J. P. a. M. Z. Krzysztof Sibilski, "Comparative Evaluatio0n of Power Requirements for Fixed, Rotary and Flapping Wings Micro Air Vehicles," in *AIAA*, Hilton Head, South Carolina, 2007. Web, 2016.

[5] A. P. a. T. J. Mueller, "Low Reynolds Number Aerodynamics of Low -Aspect-Ratio, Thin/Flat/Chambered-Plate Wings," *AIAA,* Vols. 37, N0.5S, no. September-October, pp. 825-832, 2000.

[6] G. E. T. a. T. J. Mueller, "Low-Aspect-Ratio Wing Aerodynamics at Low Reynolds Numbers," *AIAA,* vol. 42, no. No.5, pp. 865-873, 2004.

[7] M. G.-e. a. C.-M. Ho, "The Pitching Delta Wing," *AIAA Journal,* vol. 23, no. No. 11, pp. 1660-1665, 1985.

[8] D. J. I. Michael I. Friswell, "Morphing concepts for UAVs," in *21st Bristol UAV Systems Conference*, 2006.

[9] H. G. a. R. L. Mujahid Abdulrahim, "Flight Characteristics of Shaping the Membrane Wing of a Micro Air Vehicle," *Journal of Aircraft,* vol. 42, no. No. 1, pp. 131-137, 2005.

[10] M. Gad-el-Hak, "Micro-Air-Vehicles: Can They be Better Controlled," *Journal of Aircraft,* vol. 38, no. No. 3, pp. 419-429, 2001.

[11] K. K. E. C. D. A. J. K. D. J. I. Onur Bilgen, "Morphing Wing Micro-Air_vehicle via Macro-Fiber-Composite Actuators," in *48th AIAA/ASME/ASCE/AHS/ASC*

Structures, Structural Dynamics, and Materials Conference, Honolulu, Hawaii, 2007.

[12] M. F. R. M. V. O. J. F. I. B. a. M. S. Anothony M. DeLuca, "Experimental Investigation into the Aerodynamic Properties," in *24th AIAA Aerodynamic Measurement Technology and Ground Testing Conference*, Portland, Oregon, 2004.

[13] S. W. S. Jamey D. Jacob, "Design Limitations of Deployable Wings," in *47th AIAA Aerospace Sciences Meeting Including The New Horizons Forum and Aerospace Exposition*, Orlando, Florida, 2009.

[14] R. H. a. B. N. Glen Brown, "Inflatable Structures for Deployable Wings," American Institute of Aeronautics &Astronautics, 2001.

[15] J.-M. M. a. C. Thipyopas, "Aerodynamic Performance of a Biplane Micro Air Vehicle," *Journal of Aircraft,* vol. 44, no. No.1, pp. 291-299, 2007.

[16] Keennon, Joel M. Grasmeyer and Mathew T., "Developement of the Black Widow Micro Air Vehivle," *AIAA,* pp. 1-9, 2001.

[17] M. T. S. a. D. K. Wong, "Design and Developement of a Micro Air Vehicle (MAV) Concept: Project Bidule," University Of Sydney, Sydney, 2006 IT a paper on the Sydney.edu site.

[18] D. J. P. a. F. Bohorques, "Challenges Facing Future Micro-Air-Vehicle Developement," *Journal of Aircraft,* vol. 43, no. No. 2, pp. 290-305, 2003.

[19] R. v. Mises, Theory of Flight, New York: Dover Publications, Inc., 1959.

[20] J. John D. Anderson, Aircraft Performance and Design, New York: The McGraw-Hill Companies, Inc, 1999.

Timothy James Schutter was born in Princeton Junction, New Jersey on March 11th 1991 to Kenneth Schutter and Kristin Keller. He graduated from Kimberton Waldorf School after twelve years in 2010 and attended Rochester Institute of Technology to study Industrial Design. After a year, Tim, transferred to Lehigh University and received a Bachelors of Science in Mechanical Engineering in 2014. He has stayed on at Lehigh to continue his studies and complete a Master's of Science in Mechanical Engineering.